International Journal of Mechanical Sciences 296 (2025) 110339

Contents lists available at ScienceDirect

International Journal of Mechanical Sciences

journal homepage: www.elsevier.com/locate/ijmecsci

Inelastic and fracture behaviour of nuclear graphite

K. Irman [a,b], E.A. Flores-Johnson [a,b,*], J.J. Kruzic [b], W.E. Windes [c], T.J. Marrow [d], O. Muránsky [a,b,*]

[a] Australian Nuclear Science and Technology Organisation (ANSTO), Lucas Heights, NSW 2234, Australia
[b] School of Mechanical and Manufacturing Engineering, University of New South Wales (UNSW Sydney), Sydney, NSW 2052, Australia
[c] Idaho National Laboratory, Idaho Falls, ID 83415, USA
[d] Department of Materials, University of Oxford, Parks Road, Oxford OX1 3PH, United Kingdom

ARTICLE INFO

Keywords:
Tensile strength
Fracture behaviour
Finite element simulation
Nuclear graphite
Concrete damaged plasticity model
Dilation angle

ABSTRACT

Understanding nuclear graphite's inelastic and fracture behaviour is essential for current and future reactor technologies using graphite-based engineering components. This study compares the behaviour of three nuclear graphite grades, fine-grained IG-110, coarse-grained NBG-18 and medium-grained PCEA, subjected to the uniaxial compression (UC) and the splitting tensile (ST) tests. It was found that the IG-110 graphite has a more favourable combination of ultimate strength and ductility when compared to the NBG-18 and PCEA grades containing large pores acting as strain concentrators. The formation of shear cracks was the primary failure mode under compression, while the formation of a main tension crack in the middle of the specimen was the primary failure mode during the ST test. The inelastic and fracture response was modelled using finite element simulations employing the concrete damaged plasticity (CDP) material model with the dilation angle parameter value selected by two different optimisation processes; a decoupled optimisation was run on the UC and ST models separately, and a coupled optimisation was performed on the UC and ST models running simultaneously. The best predictions were obtained when the value from the coupled optimisation was used. The results showed that the CDP model accurately describes the inelastic behaviour and peak force of all graphite grades and could also capture the failure modes observed experimentally in both UC and ST tests. In particular, the numerical model could capture the crack initiation and propagation path observed in the ST test reasonably well for the IG-110 and PCEA graphite grades.

1. Introduction

Graphite is utilised extensively in the nuclear industry as a key neutron-moderating material of various nuclear reactor designs that exploit its low neutron absorption and large scattering cross-section [1,2]. The next generation of reactor systems utilising a graphite neutron moderator is expected to operate at temperatures of up to 1000 °C under a significant flux of high-energy particles [3–6]. These extreme operating conditions lead to irradiation-induced dimensional changes and associated stresses [7–9], which in turn may cause the formation and propagation of macroscopic cracks, resulting in the loss of the structural integrity of graphite components [10–12]. In its unirradiated condition, graphite exhibits a quasi-brittle behaviour; however, irradiation increases its stiffness and apparent brittleness [13–17]. An in-depth understanding of the mechanical behaviour of graphite is thus critical for the structural integrity assessment of graphite components [18–22], as these can be the life-limiting components of the overall system.

In general, the bulk mechanical properties of graphite are governed by the multi-phase microstructure containing filler particles, binder (pitch), and a large number of defects such as open and closed porosity that typically constitute up to ~20 % of its volume [16,23–27]. As noted by several authors, the microstructure of graphite resembles the microstructure of other porous aggregate materials such as concrete and rock [28,29]. The porosity in graphite has a size distribution across many length scales, from microcracks [30–32] to larger gas pores [33–35]. Unirradiated graphite exhibits an initial linear elastic behaviour followed by a non-linear inelastic behaviour, which is somewhat similar to the elastoplastic response of alloys. The irreversible inelastic deformation of graphite is attributed to the propagation and accumulation of microcracks [36,37] and pre-existing defects [38,39], which ultimately coalesce, leading to macroscopic fracture [40,41]. During crack propagation, a micro-cracked fracture process zone is formed

* Corresponding authors at: Australian Nuclear Science and Technology Organisation (ANSTO), Lucas Heights, NSW 2234, Australia.
E-mail addresses: floresje@ansto.gov.au (E.A. Flores-Johnson), ondrej.muransky@ansto.gov.au (O. Muránsky).

https://doi.org/10.1016/j.ijmecsci.2025.110339
Received 5 February 2025; Received in revised form 10 April 2025; Accepted 30 April 2025
Available online 1 May 2025

ahead of the crack tip, leading to the quasi-brittle nature of graphite fracture [15,42]. Hence, the structural properties of graphite can be linked to the stability of the microcracks, which is directly related to its microstructure [33,42,43]. In addition, the inherently brittle nature of the carbon structures present in graphite also contributes to its nonlinearity and fracture behaviour [44–48].

A wide range of engineering applications utilising graphite components requires reliable predictions of the inelastic behaviour of graphite under various in-service loading conditions. These predictions are challenging due to the complex microcracking and porosity-driven inelastic behaviour, which is difficult to describe through empirical models [42]. Moreover, the mechanical behaviour of graphite in compression is very different from that in tension. For instance, the ultimate strength in compression could be 3 to 4 times higher than that in tension [49,50]. Another material that exhibits different behaviour in compression compared to its behaviour in tension is concrete [51,52] due to its inherently porous and granular microstructure [53,54]. An approach for describing the inelastic and fracture behaviour of graphite could include employing a constitutive material model that has been applied to predict the mechanical behaviour of other porous aggregate materials, such as concrete or rocks, considering that similar fracture mechanisms observed for graphite have also been observed in these quasi-brittle materials [55–57].

Among constitutive material models that have been implemented in finite element (FE) codes to predict the mechanical behaviour of concrete and other quasi-brittle materials, the concrete damaged plasticity (CDP) model has been widely used due to its capability to model inelastic behaviour under different loading conditions, including compression and tension, as well as irreversible damage [58–60]. The CDP material model, first developed by Lubliner et al. [61] and later modified by Lee and Fenves [62], is a plasticity-based damage model that accounts for the evolution of the strength under tension and compression and identifies the failure of the material into either compressive crushing or tensile cracking [58]. The CDP model has been primarily used to model concrete [63–68]; however, it has also been successfully used to model other quasi-brittle materials such as mortar [69,70], plaster [71], masonry [72,73] and graphite [55,74].

Becker and Marrow [55] applied the CDP model in their 2D FE simulations to capture the mechanical behaviour of unirradiated Gilsocarbon graphite compact tension (CT) specimens and notched specimens under three-point bending using plane stress conditions. They found that the FE simulations with the CDP model captured the general mechanical behaviour of both specimens, including damage localisation and material degradation after the peak load. In another study, Wigger et al. [74] used the CDP material model in the 3D FE analysis of a Gilsocarbon Brazilian disc specimen with a notch subjected to diametral compression, assuming a stationary crack with no crack growth. From their FE results, they could estimate the J-integral from the near-tip strains of the notch. Multiscale modelling has also been used to model graphite [75–78]. Multiscale models could lead to more accurate results for small testing specimens [79,80]; however, these models take more time to build and require extensive computational resources due to the large number of elements used to capture the features of the graphite microstructure. Therefore, this modelling approach is unsuitable for dimensionally larger engineering components where a continuum-based FE model would be more appropriate.

Based on the literature above, there is still a need for more exploration of the applicability of the constitutive CDP model to be used in a continuum-based FE model to capture the mechanical behaviour of nuclear-grade graphite under compression and tension loading. In this work, first, the compressive and tensile behaviour of the fine-grained (IG-110), medium-grained (PCEA), and coarse-grained (NGB-18) nuclear graphite grades are examined experimentally using the uniaxial compression (UC) test and the splitting tensile (ST) strength test. These three graphite grades are among the candidate grades that were selected for the very-high-temperature reactor (VHTR) based on their properties [43,81,82]. The VHTR is a graphite-moderated nuclear reactor and is one of the Generation IV nuclear reactors being developed for energy generation [83–85]. Second, the mechanical response of the tested graphite grades is modelled using continuum-based FE simulations employing the CDP material model to capture the inelastic and fracture responses. Then, to find the unknown material parameter, the dilation angle, of the CDP model, an optimisation process is used, in which the FE simulations are iteratively compared with the experimental load-displacement measurements of the UC and ST tests via objective functions until a good agreement is achieved. Finally, the FE simulations are used to investigate the capability of the CDP model to predict the failure modes and crack development of the studied graphite grades subjected to the UT and ST tests.

The paper's outline is as follows: Section 2 presents the materials used in this work and the experimental methodology employed to perform the UT and ST tests. Section 3 presents the FE simulations and CDP material model employed to simulate the UT and ST tests and the optimisation process. Section 4 presents and discusses the experimental testing results, the FE simulation and optimisation results, and a failure analysis based on experimental observations and numerical predictions. Finally, Section 5 presents the conclusions drawn from the results of this investigation.

2. Materials and experimental methods

This section presents the three nuclear graphite grades studied in this work, as well as their properties and microstructure. The experimental methodology used to perform the mechanical testing, i.e., the UT and ST tests, is also presented along with the digital image correlation (DIC) analysis used during the ST test.

2.1. Materials

Three nuclear-grade graphites, (i) fine-grained IG-110, (ii) coarse-grained NBG-18, and (iii) medium-grained PCEA grades provided by the Idaho National Laboratory (INL) in Idaho Falls (USA), were tested to measure their compressive and splitting tensile responses. Fig. 1 shows the scanning electron microscopy (SEM) images comparing their overall microstructures. It can be seen in Fig. 1 that the fine-grained IG-110 has a large number of fine pores (< 15 μm) [86]. In contrast, PCEA and NBG-18 graphite grades have a smaller number of significantly larger pores, which are often hundreds of micrometres in size. Table 1 summarises the microstructural, physical, and mechanical properties of these graphite grades found in the literature.

2.2. Mechanical testing

Two different experimental tests were performed on the graphite samples. First, UC testing was performed on cylindrical graphite specimens to determine the compressive material properties and validate the numerical models. Second, the ST strength test was performed on disc specimens to validate the numerical models and indirectly estimate the tensile strength. The experimental details for both tests are described in the following sections.

2.2.1. Uniaxial compression test

The UC test of cylindrical specimens with a diameter of 12.7 mm and 20 mm in height was performed according to the ASTM D7012 standard [107] using an Instron universal testing machine with a constant displacement rate of 0.015 mm/min (Fig. 2a). The test specimens were cut from as-received blocks using electrical discharge machining (EDM). The compression plates were lubricated using molybdenum disulphide to minimise friction between specimens and compression plates. At least four specimens of each graphite grade were tested up to the fracture point. The strain measurement during the testing was monitored via a linear variable displacement transducer (LVDT) attached to the Instron

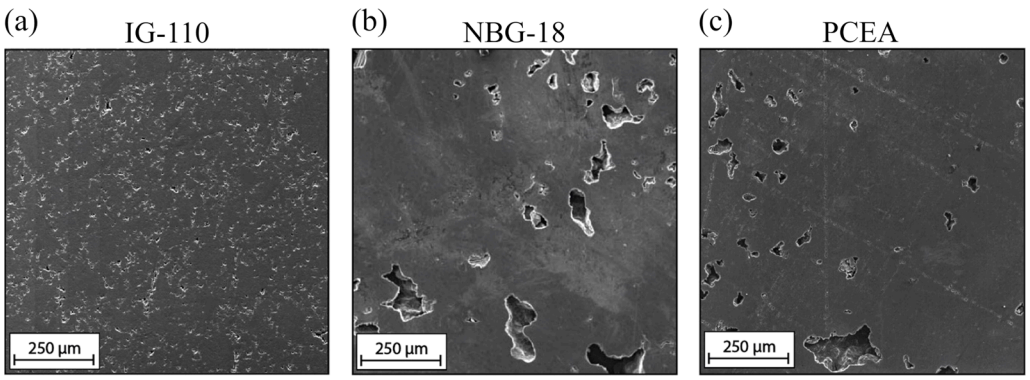

Fig. 1. SEM images of studied graphite grades showing their overall microstructures: (a) IG-110 is fine-grained, (b) NBG-18 is coarse-grained, and (c) PCEA is medium-grained.

Table 1
Reported microstructural, physical, and mechanical properties of IG-110, NBG-18 and PCEA graphite grades.

Properties	IG-110	NBG-18	PCEA
Grain size (μm)	10–25 avg. [87,88] <100 max. [89]	300–360 avg. [21,26] 1600–1800 max. [21,26]	360 avg. [21] 760–800 max. [90,91]
Bulk density (g/cm^3)	1.75–1.77 [21,92]	1.85–1.88 [21,93]	1.83–1.85 [21,94]
Porosity (%)	14.73–21.7 [26,95]	13.97–16.8 [26,95]	15.98–16.9 [12,26]
Young's modulus (GPa)	7.9–9.8 [96,97]	10.74–12.37 [82,98]	9.23–10.75 [82,98]
Poisson's ratio (–)	0.138–0.210 [77,99]	0.230 [99]	0.178 [99]
Compressive strength (MPa)	69.6–86.4 [92,100]	73.5–82.85 [98,100]	62.99–69.89 [98,101]
Tensile strength (MPa)	22.0–29.6 [49,102]	20.4–24.07 [13,98]	15.32–23.5 [98,103]
Fracture energy (J/m^2)	180–250 [39,55,104–106]	180–250 [39,55,104–106]	180–250 [39,55,104–106]

machine crosshead, as shown in Fig. 2a.

2.2.2. Splitting tensile test

The ST test was performed following the ASTM D8289 standard [108], which is dedicated to the ST testing of nuclear graphite grades. The ST test is an indirect method to estimate the tensile strength of brittle materials such as rocks, ceramics, or graphite, which are difficult to test under uniaxial tension conditions. During the ST test, a thin disc is compressed diametrically; the compression load induces tensile stresses in the centre of the disc specimen in the direction perpendicular to the loading. The tensile stresses then lead to specimen failure by disc splitting [109,110]. The ST test setup is shown in Fig. 2b The loading fixture used in this work (Fig. 2b), designed according to [108], allows testing of complete round disc specimens as opposed to flattened discs [111] that could lead to stress concentrations at the contact surface between the specimen and loading plates. The current study used disc specimens with a diameter of 12.7 mm and a thickness of $L = 6.35$ mm cut with EDM. Both flat faces of the disc specimens were gently polished to reduce the effect of the post-cutting roughness on the DIC analysis. The ST tests were done using an Instron universal testing machine at a constant displacement rate of 0.015 mm/min until the specimens failed. The displacement was measured using an LVDT (Fig. 2b). The splitting tensile strength σ_{tu} was calculated using the following equation [108]:

$$\sigma_{tu} = 0.931 \frac{P}{\pi LR}, \tag{1}$$

where P is the maximum applied load, and R is the specimen radius. The in-plane strain fields at the disc surface were measured using the 2D DIC technique during the ST test. For these measurements, a black and white speckle pattern (white painted background with black speckles) was

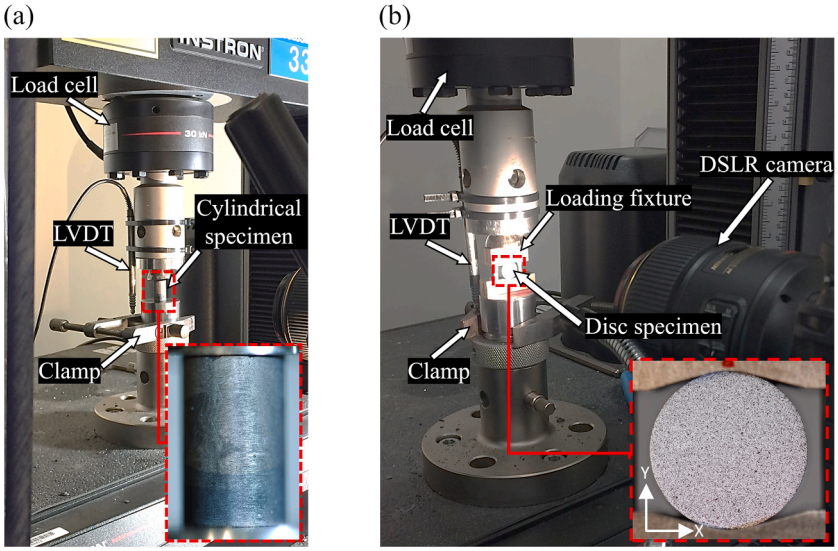

Fig. 2. Mechanical testing of the nuclear graphite grades: (a) UC test setup for cylindrical specimens and (b) ST test setup for disc specimens.

created on one of the polished disc specimen faces using an airbrush (Iwata Revolution, Anest Iwata, Japan) and water-based inks (FW Acrylic Ink, Daler-Rowney, UK). A single Nikon D500 DSLR camera with a macro lens (AF-S 105 mm Micro-Nikkor) was used; this configuration had a depth of field of ± 5 mm. The images were recorded every second during the testing. To follow the evolution of the strain field in the specimen X-Y plane (Fig. 2b), the recorded image sequences were analysed using the GOM Correlate 2021 software package [112]. It is noted that the out-of-plane displacement in the Z direction (Fig. 2b) was not captured. At least seven specimens of each graphite grade were subjected to the ST test.

3. Numerical modelling and optimisation

This section presents the numerical modelling methodology and the CDP material model used in this work. The FE simulations of the UC and ST tests of the studied graphite grades were performed in ABAQUS/Standard (version 2024) [113]. The FE simulations were coupled with the optimisation tool Isight (version 2024) [114] for the optimisation of the unknown dilation angle parameter of the CDP material model, which was used in the FE models to predict the inelastic and fracture behaviour of the graphite grades. The following subsections explain in detail the FE simulations and the optimisation process.

3.1. FE simulations

3.1.1. FE models and mesh convergence study

Fig. 3a and b show the 3D FE models of the UC and ST tests, respectively, developed in Abaqus/Standard (Version 2024) [113]. Both FE models were loaded in the Y direction, as seen in Fig. 3. Due to symmetry, only a quarter model was built for both UC and ST simulations to reduce computational cost (Fig. 3). In addition, Fig. 3c shows an FE model, in which, coupled UC and ST models were run simultaneously for the optimisation process described in Section 3.2. The FE mesh comprised reduced-integration 8-node brick elements (C3D8R) for the graphite specimens and 3D rigid elements (R3D4) for the loading fixtures, which were modelled as rigid surfaces. Global element sizes of 0.7 mm and 0.2 mm were used for the UC and ST test models, respectively, based on a mesh sensitivity analysis presented below. The mesh depicted in Fig. 3 is a coarser mesh for illustration purposes. The tangential contact between the graphite specimens and loading fixtures was modelled as frictionless. The elastic response of the studied graphite grades was described using an isotropic elastic model with the elastic parameters shown in Table 2, which were selected based on parameters available in the open literature (Table 1). This approach was used considering that nuclear graphite grades are designed to be isotropic or near isotropic [94], having isotropic ratio ranges of 1.00–1.10 and 1.10–1.15, respectively [115]; for a material with an isotropy ratio of 1, properties are the same in any tested direction. IG-110 is considered an isotropic nuclear graphite grade [4], while NBG-18 and PCEA are near isotropic grades [26]. The inelastic response of the graphite grades was modelled using the CDP model, described in detail in the following subsections.

A mesh sensitivity analysis was conducted for UC and ST test simulations using element sizes ranging from 0.1 mm to 2 mm. The relative percentage difference R_{pd} of the peak force for different element sizes was utilised to assess mesh convergence. Fig. 4a and b show R_{pd} for the UC and ST simulations, respectively, which was calculated as:

$$R_{pd} = \frac{\left|P_{\max\_f} - P_{\max\_c}\right|}{\left[\frac{\left(P_{\max\_f} + P_{\max\_c}\right)}{2}\right]} \times 100\%, \tag{2}$$

where $P_{\max\_f}$ is the predicted peak force using the finer mesh, and $P_{\max\_c}$ is the predicted peak force using coarser element sizes. The normalised running simulation time using a workstation with 16 cores is also pre-

Table 2
Material properties and CDP model parameters for IG-110, NBG-18 and PCEA graphite grades.

Properties	IG-110	NBG-18	PCEA
Elastic properties			
Density ρ (kg/m^3)	1770	1870	1820
Young's Modulus E_0 (GPa)	9.8	11.1	10.0
Poisson's Ratio ν (-)	0.21	0.23	0.18
Plasticity parameters			
Optimised dilation angle ψ_{ct} (°)	43.2	44.6	43.6
Eccentricity ε (-)	0.1	0.1	0.1
r_σ (-)	1.16	1.16	1.16
K_c (-)	0.667	0.667	0.667
Viscosity μ (-)	0.0005	0.0005	0.0005
Compressive behaviour			
Compressive yield stress σ_{cy} (MPa)	22.7	21.7	15.0
Compressive strength σ_{cu} (MPa)	77.7	78.2	67.1
Tensile behaviour			
Tensile strength σ_{tu} (MPa)	27.6	20.8	19.4
Fracture energy G_f (J/m^2)	220	220	220

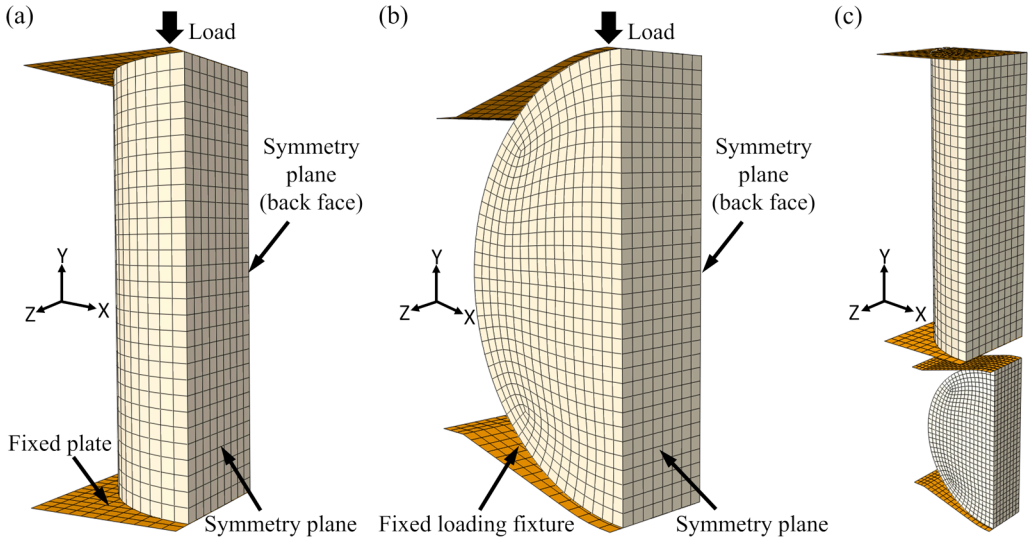

Fig. 3. Mesh of the 3D FE models: (a) UC test model, (b) ST test model and (c) coupled UC and ST models.

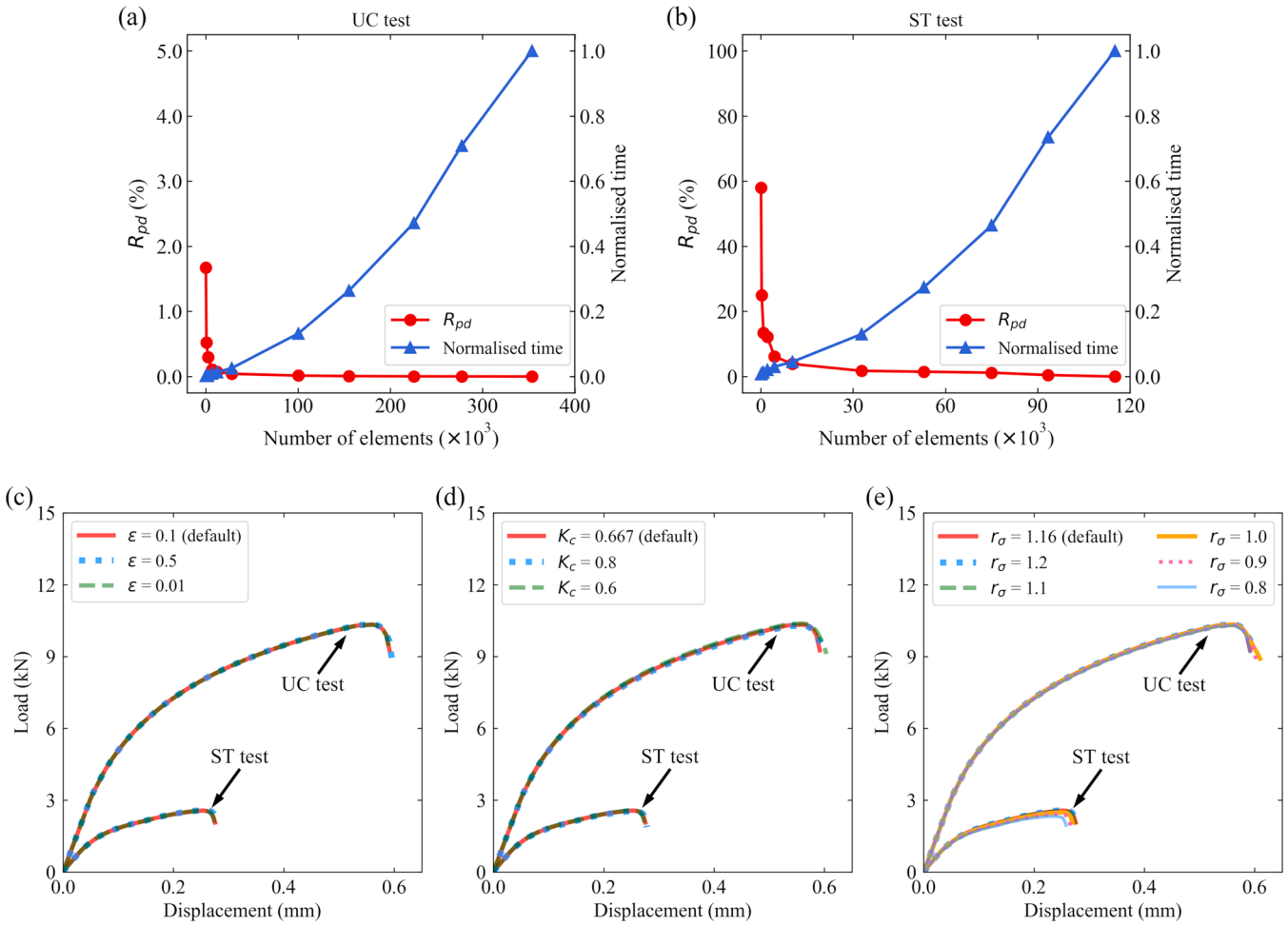

Fig. 4. Relative percentage difference R_{pd} of the peak force and normalised simulation time versus the number of elements in the simulation: (a) UC test and (b) ST test simulations. Predicted force-displacement curves of the UC and ST test simulations of the IG-110 graphite using different CDP model parameter values: (c) ε, (d) K_c and (e) r_σ.

sented in Fig. 4a and b. Mesh convergence is achieved when a decrease in element size results in $R_{pd} < 2$ %. It can be seen in Fig. 4a that mesh convergence is achieved even for the coarser mesh in the case of the UC simulations. However, an element size no larger than 0.3 mm is required for the ST simulation to achieve mesh convergence. Based on this analysis, mesh sizes of 0.7 mm and 0.2 mm were used for the UC and ST test simulations, respectively, for convergence and optimised computational efficiency.

3.1.2. *Concrete damaged plasticity model: yield surface and flow rule*

The CDP material model was used to simulate the inelastic response and damage of the tested graphite specimens. The CDP model can be used to model the inelastic behaviour and damage of concrete [116] and other quasi-brittle materials such as mortar [69] or graphite [55]. The CDP model utilises the yield function proposed by Lubliner et al. [61], which was later modified by Lee and Fenves [62] to account for the evolution of the strength under tension and compression [113]. The evolution of the yield surface is controlled by the tensile and compressive plastic hardening variables $\tilde{\varepsilon}_t^{pl}$ and $\tilde{\varepsilon}_c^{pl}$. The yield function is defined as [113]:

$$F = \frac{1}{1-\alpha}\left(\bar{q} - 3\alpha\bar{p} + \beta\left(\tilde{\varepsilon}_t^{pl}\right)\langle\hat{\bar{\sigma}}_{max}\rangle - \gamma\langle\hat{\bar{\sigma}}_{max}\rangle\right) - \hat{\bar{\sigma}}_c\left(\tilde{\varepsilon}^{pl}\right) = 0, \tag{3}$$

where $\hat{\bar{\sigma}}_{max}$ is the maximum principal effective stress, and α, β and γ are dimensionless constants defined as follows:

$$\begin{cases} \alpha = \dfrac{r_\sigma - 1}{2r_\sigma - 1}, 0 \le \alpha \le 0.5 \\ \beta = \dfrac{\bar{\sigma}_c\left(\tilde{\varepsilon}_c^{pl}\right)}{\bar{\sigma}_t\left(\tilde{\varepsilon}_t^{pl}\right)}(1-\alpha) - (1+\alpha) \\ \gamma = \dfrac{3(1-K_c)}{2K_c - 1} \end{cases}, \tag{4}$$

where, $r_\sigma = \sigma_{b0}/\sigma_{c0}$ is ratio of the initial equibiaxial compressive yield stress to the initial uniaxial compressive yield stress, $\bar{\sigma}_c\left(\tilde{\varepsilon}_c^{pl}\right)$ is the effective compressive cohesive stress, $\bar{\sigma}_t\left(\tilde{\varepsilon}_t^{pl}\right)$ is the effective tensile cohesive stress, and K_c is the ratio of the second stress invariant on the tensile meridian to that on the compressive meridian [61] at initial yield for any given value of the pressure invariant p. The CDP model assumes a non-associated potential plastic flow. The flow potential used for the CDP model is the Drucker-Prager hyperbolic function [113]:

$$G = \sqrt{(\epsilon\sigma_{tu}\tan\psi)^2 + \bar{q}^2} - \bar{p}\tan\psi, \tag{5}$$

where, σ_{tu} is the uniaxial tensile stress at failure, ε is the eccentricity parameter, ψ is the dilation angle measured in the $\bar{p}$–$\bar{q}$ plane at high confining pressure; $\bar{q}$ is the von Mises effective equivalent stress and $\bar{p}$ is the hydrostatic pressure stress.

The abovementioned material parameters (ψ, ε, r_σ and K_c) are

required inputs for the CDP model in Abaqus/Standard. The default values of $\varepsilon = 0.1$, $r_\sigma = 1.16$ and $K_c = 0.667$ were used [113] (see Table 2), while the dilation angle ψ was optimised, as described in Section 3.2. To assess the influence of ε, r_σ and K_c on the graphite's mechanical response, Fig. 4c–e present the predicted force-displacement curves from both UC and ST test simulations for the IG-110 graphite, using parameter ranges commonly found in the literature for concrete [65,117]. These figures show that variations in ε, K_c and $r_\sigma \geq 1.1$ have a minimal effect on the predicted mechanical response up to the peak load. Reducing r_σ below 1.1 has some effect on the post-failure response in compression but no effect on the peak load; however, it lowers the ST peak force (Fig. 4c). While reported r_σ values for concrete typically fall between 1.1 and 1.2 [65], data for the equibiaxial compressive yield strength of concrete still remains scarce [117], and in the case of graphite, even more so, as no experimental measurements of equibiaxial compressive yield strength were found in the open literature. Although some studies suggest r_σ could be <1 for graphite [55], the equibiaxial behaviour of graphite is still not well understood [118]. Given the absence of reliable experimental data of r_σ for the studied graphite grades and the sensitivity study results shown in Fig. 4c–e, the default Abaqus/Standard parameters $\varepsilon = 0.1$, $r_\sigma = 1.16$ and $K_c = 0.667$ were used as a reasonable approximation for modelling purposes.

The dilation angle ψ, which controls the amount of volumetric strain developed during inelastic deformation, is an unknown parameter for the studied graphite grades. The values of ψ for the CDP model must be in the range of $0^\circ < \psi < 56.3^\circ$ [113]. Values for ψ in the range of $20^\circ - 50^\circ$ are commonly accepted for concrete [119]. While a value of $\psi = 30^\circ$ was used in the FE simulations of Gilsocarbon graphite CT specimens [55], the open literature has not yet reported a range of ψ values for nuclear-grade graphite modelling when subjected to compressive and tensile loads. In this work, ψ is optimised for the graphite grades investigated here using the optimisation process described in Section 3.2; the optimised values are shown in Table 2, while the complete results of the optimisation process are presented in Section 4.2. Finally, the CPD model requires the viscosity parameter μ for viscous regularisation, considering that material models exhibiting softening behaviour and stiffness degradation could lead to convergence problems. The value of μ should be small compared to the characteristic time increment of the simulation to improve convergence without altering the simulation results [113]. Here, a value of μ=0.0005 was used.

3.1.3. Concrete damaged plasticity model: inelastic behaviour

In the CDP model, the uniaxial compression response is linear elastic until the initial compressive yield stress σ_{cy} is reached. In the inelastic regime, the response is characterized by stress hardening followed by strain softening beyond the ultimate compressive stress σ_{cu} (Fig. 5a) [113]. The values of σ_{cy} and σ_{cu} used for the CDP model are shown in Table 2, which were taken from the mean values obtained experimentally in Section 4.1.1. The compressive stress σ_c beyond the elastic regime is required for the CDP model as a tabular function of the inelastic strain $\tilde{\varepsilon}_c^{in}$, defined as $\tilde{\varepsilon}_c^{in} = \varepsilon_c - \varepsilon_{0c}^{el}$, where $\varepsilon_{0c}^{el} = \sigma_c / E_0$ (Fig. 5a). E_0 is the initial elastic modulus of the material. Under uniaxial tension, the stress-strain response is linear elastic until the failure stress σ_{tu}, corresponding to the onset of microcracking, is reached. Beyond σ_{tu}, the response is characterized by strain softening (Fig. 5b). The post-failure behaviour can be defined by providing the post-failure tensile stress σ_t in tabular form as a function of the cracking strain $\tilde{\varepsilon}_c^{ck} = \varepsilon_t - \varepsilon_{0t}^{el}$, where $\varepsilon_{0t}^{el} = \sigma_t / E_0$ (Fig. 5b). However, for brittle materials with no reinforcement, the post-failure response in tension in the CDP model should be provided by specifying σ_t as a tabular function of the cracking displacement u_t^{ck} to avoid unreasonable mesh sensitivity in the results [113]. Alternatively, the fracture energy G_f can be specified directly as a material property, assuming a linear loss of strength after the failure strength (Fig. 5c).

3.1.4. Concrete damaged plasticity model: damage

When material damage is not considered to describe the mechanical response beyond the elastic regime, the abovementioned description of inelastic behaviour will suffice. However, concrete is a material that undergoes damage before catastrophic failure in the form of tensile cracking and compressive crushing [120]. Similarly, damage in graphite occurs before failure via the development and accumulation of microcracks [29,41,121]. Microcracks eventually grow, resulting in catastrophic failure. The CDP model considers material damage by incorporating stiffness and strength degradation via the damage variables d_c and d_t for compressive and tensile behaviour, respectively. The damage variables take values from 0 (undamaged material) to 1 (total loss of strength). When damage is considered, the stress-strain relationships in compression and tension loading can be expressed as [113]:

$$\begin{cases} \sigma_c = (1 - d_c) E_0 \left(\varepsilon_c - \tilde{\varepsilon}_c^{pl} \right) \\ \sigma_t = (1 - d_t) E_0 \left(\varepsilon_t - \tilde{\varepsilon}_t^{pl} \right) \end{cases}, \tag{6}$$

where the terms $(1 - d_c)E_0$ and $(1 - d_t)E_0$ represent the reduction of the elastic modulus in terms of the damage variables d_c and d_t, respectively (Fig. 5a and b).

For the compression part of the CDP model, damage data should be provided in tabular form as a $d_c - \tilde{\varepsilon}_c^{in}$ curve so the FE software internally converts the inelastic strain to compressive plastic strain $\tilde{\varepsilon}_c^{pl}$. For the tension part of the CDP model, when damage data is provided as a

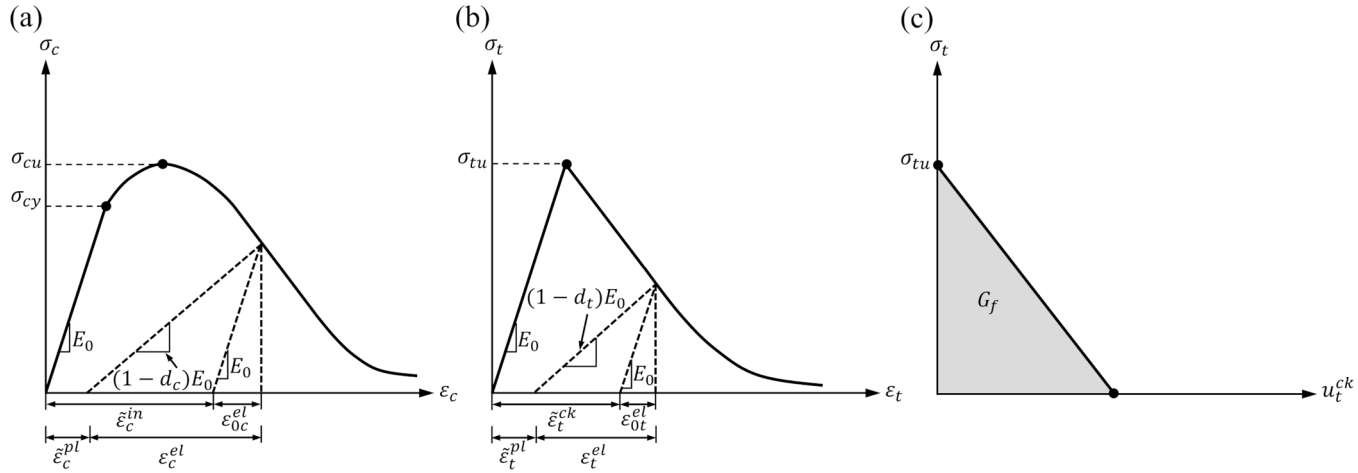

Fig. 5. CDP material model: stress-strain response under (a) uniaxial compression and (b) uniaxial tension; (c) post-failure tensile stress-displacement curve.

tensile damage $d_t - \tilde{\varepsilon}_t^{ck}$ curve, the tensile plastic strain $\tilde{\varepsilon}_t^{pl}$ is computed by the FE software. $\tilde{\varepsilon}_c^{pl}$ and $\tilde{\varepsilon}_t^{pl}$ are computed by the FE software as follows:

$$\begin{cases} \tilde{\varepsilon}_c^{pl} = \tilde{\varepsilon}_c^{in} - \dfrac{d_c}{(1-d_c)}\dfrac{\sigma_c}{E_0} \\ \tilde{\varepsilon}_t^{pl} = \tilde{\varepsilon}_t^{ck} - \dfrac{d_t}{(1-d_t)}\dfrac{\sigma_t}{E_0} \end{cases}. \tag{7}$$

For the case of unreinforced materials, the fracture energy G_f should be used to specify the post-failure tensile response, assuming a linear loss of strength, as previously mentioned. In this case, damage is provided in tabular form as a $d_t - \tilde{u}_t^{ck}$ curve. The cracking displacement $\tilde{u}_t^{ck}$ at which complete loss of strength occurs, i.e., $d_t = 1$, can be calculated as [113]:

$$\tilde{u}_t^{ck} = 2G_f/\sigma_{tu}. \tag{8}$$

In this case, the FE software computes the plastic displacement $\tilde{u}_t^{pl}$ as follows:

$$\tilde{u}_t^{pl} = \tilde{u}_t^{ck} - \frac{d_t}{(1-d_t)}\frac{\sigma_t l_0}{E_0}, \tag{9}$$

where l_0 is the characteristic length associated with the integration points, computed as $l_0 = \sqrt[3]{V_e}$; V_e is the element volume. l_0 should be specified directly in the Abaqus input file in the CDP model keyword as *Concrete Damaged Plasticity, REF LENGTH=l_0; defining l_0 is not supported in the Abaqus/CAE interface [113].

The CDP model assumes that no damage occurs before the tensile strength for the material tensile response, making the estimation of the $d_t - \tilde{u}_t^{ck}$ curve for the tensile damage definition a straightforward process when G_f is used to specify the post-failure tensile response considering a linear loss of strength (Eq. (8)) [113]. The values of G_f and σ_{tu} used in Eq. (8) for the CDP model are shown in Table 2. A value of G_f=220 J/m^2 (Table 2) was selected for all graphite grades based on reported values in the literature [39,55,104–106]. It is mentioned that the constant value of G_f was selected, considering this parameter would mainly affect the post-failure response, which was not quantitatively assessed in this work. In addition, some preliminary simulations showed that G_f does not affect the UC peak load, while only a small effect of <1.5 % on the predicted ST peak load was observed when G_f values of 180 J/m^2 or 250 J/m^2 were used (see Table 1). The values of σ_{tu} for the NBG-18 and PCEA grades (Table 2) were taken from the mean values obtained experimentally in Section 4.1.1; however, the value of σ_{tu}=27.6 MPa used for the IG-110 grade (see Table 2) was taken from Zhang et al. [49] considering that the experimental value obtained in this work (σ_{tu}=22.4 MPa, see Table 4 in Section 4.1.1) was much lower than most reference values of the IG-110 tensile strength reported in the literature (25–30 MPa) [49,97,102], which is discussed in Section 4.1.1.

In contrast, calculating the $d_c - \tilde{\varepsilon}_c^{in}$ curve for the compressive damage definition is much more complex than estimating the tensile damage mentioned above. Ideally, it requires performing cyclic compression tests, which include loading and unloading cycles at different strains until failure to obtain the stiffness degradation (damage) at different deformation stages [122]. Without such experimental cyclic test data, a damage evolution law is required to estimate the damage accumulation with increasing strain. In this context, several damage evolution laws have been proposed to obtain $d_c - \tilde{\varepsilon}_c^{in}$ curves for concrete. For instance, the following simplified equation to estimate concrete damage in compression using the compressive strength as a reference for damage initiation has been employed in several studies [116,123]:

$$d_c = 1 - \frac{\sigma_c}{\sigma_{cu}}. \tag{10}$$

However, Eq. (10) assumes no compressive damage occurs before σ_{cu} is reached. In contrast, to consider damage before the compressive strength, the damage parameter for concrete in compression has been estimated as the ratio of the inelastic strain to the total strain as follows [124]:

$$d_c = \frac{\tilde{\varepsilon}_c^{in}}{\varepsilon_c}. \tag{11}$$

Another damage evolution law to account for damage occurring before the compressive strength was presented by Zhou et al. [125]. In their work, they developed an exponential law based on the well-known Mazar's damage model for concrete [126] as follows:

$$d_c = 1 - e^{-\alpha_c \frac{(\varepsilon_c - \varepsilon_{c0})}{\varepsilon_{c0}}}, \tag{12}$$

where α_c is a constant parameter, while ε_{c0} is the threshold compressive strain at which damage commences in the material.

Most damage evolution laws in the open literature have been developed for concrete. In this context, damage evolution laws for graphite are scarce. In a recent paper, Yi et al. [41] estimated the damage of graphite subjected to uniaxial compression and tension using DIC. They found that the damage rate increased steadily with increasing strain and then slightly slowed down from a particular strain until the peak strength was reached. They also found that the relationship between damage and compressive strain could be described by a polynomial function as follows:

$$d_c = -A\varepsilon_c^2 + B\varepsilon_c - C, \tag{13}$$

where *A, B* and *C* are material constants. In contrast, Morrison et al. [29] studied the damage evolution of graphite grade IG-110 subjected to uniaxial tensile loading using a discrete lattice model. They found that the damage slowly progresses at low deformation levels and progresses more rapidly when it approaches the peak load. While no damage law was proposed to describe this behaviour in their work, an exponential damage law first developed for composites can describe a similar behaviour, in which damage accumulates slowly at low deformation levels and increases more rapidly when approaching the peak strength [127,128]:

$$d_c = 1 - e^{\left[-\frac{1}{ne}\left(\frac{\varepsilon_c}{\varepsilon_{cf}}\right)^n\right]}, \tag{14}$$

where e is the base of the natural logarithm, ε_{cf} is the nominal failure strain, and n is a shape parameter. In conclusion, the damage evolution of nuclear-grade graphite is complex and revealing the mechanisms behind it to develop a law that can predict it requires extensive micromechanical studies [41]. For instance, some studies have demonstrated with direct measurements that the elastic modulus of graphite degrades with increasing applied tensile strain due to damage development [16,129].

To assess the effect of the various d_c formulations on the predicted mechanical response of graphite, FE simulations of both UC and ST tests were performed using the CDP model with different damage evolution laws. Fig. 6a shows, for the IG-110 graphite grade, the average experimental stress-strain curve and the damage variable d_c calculated using various damage evolution laws; this average experimental curve was used as input in the CDP model and for estimating d_c using Eqs. (10)–(14). Fig. 6b shows, for the IG-110 graphite grade, the predicted force-displacement curves using different damage evolution laws (Eqs. (10), (13) and (14)) along with the average experimental force-displacement curves from the UC and ST tests (these tests are presented in detail in Section 4.1.1). The predicted curve when no damage is considered is also depicted for comparison purposes in Fig. 6b. It can be seen in Fig. 6a that d_c rapidly increases from the early stages of loading when Eqs. (11)–(13) are used, as expected. On the other hand, d_c slowly increases in the early stages of loading and rapidly increases after the peak strength has been reached when Eq. (14) is used. Finally, d_c rapidly accumulates

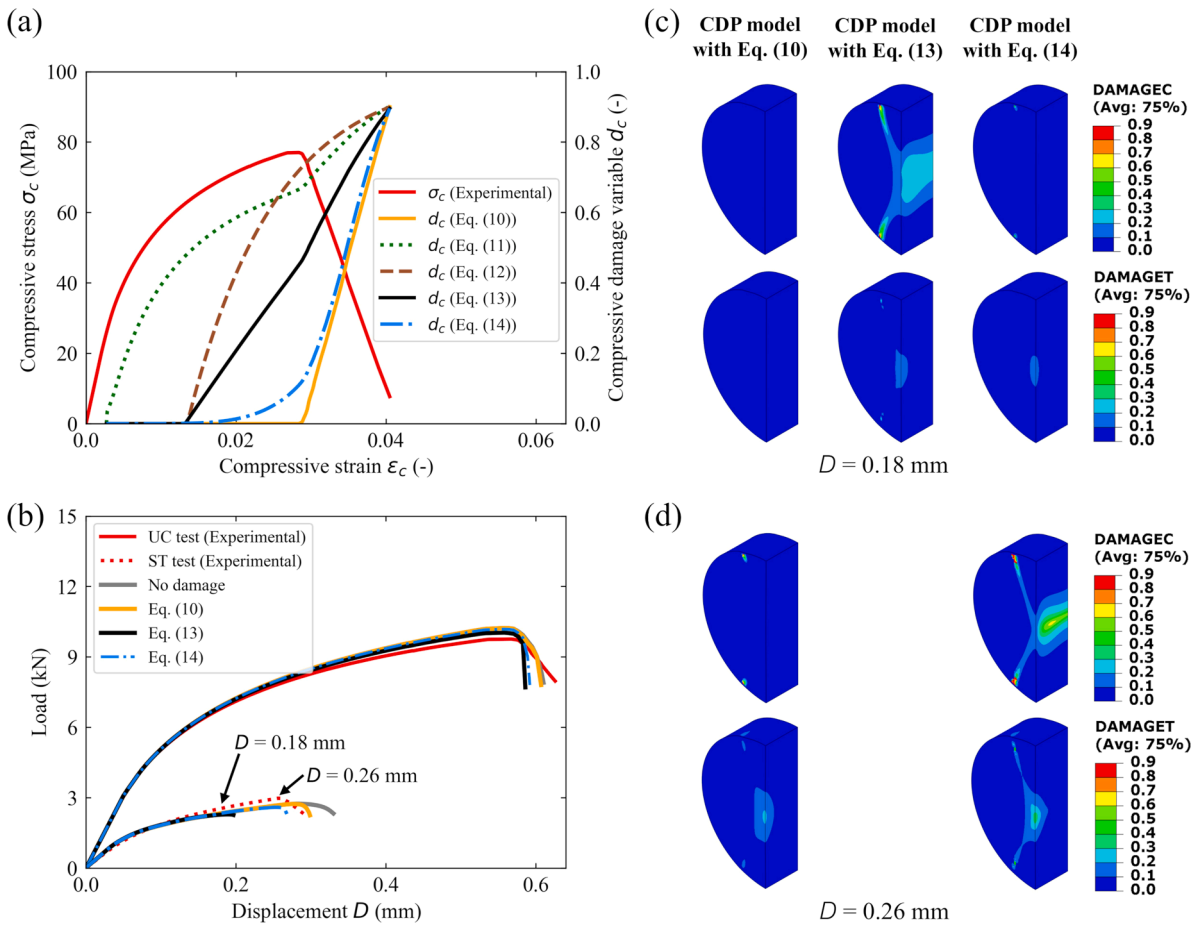

Fig. 6. (a) Estimated compressive damage variable d_c versus compressive strain for the IG-110 graphite grade using various damage evolution laws (Eqs. (10)-(14)) and average experimental stress-strain curve. (b) IG-110 graphite grade average experimental force-displacement curves from the UC and ST tests and predicted force-displacement curves using various damage evolution laws (Eqs. (10), (13) and (14)). (c) Contour plots of the compressive damage (DAMAGEC) and tensile damage (DAMAGET) output variables from the ST test simulations at displacements of 0.18 mm and 0.26 mm.

when Eq. (10) is used; however, d_c accumulation only initiates after reaching the peak load.

It can be seen in Fig. 6b that using different damage evolution laws has a slight effect on the uniaxial compressive response up to the peak force. In contrast, using different damage evolution laws dramatically affects the mechanical response of the graphite disc subjected to the splitting tensile loading. It can be seen in 6b that when damage is estimated using Eq. (13), the specimen fails prematurely at a displacement of 0.18 mm, which is much lower than the observed experimental displacement of 0.26 mm at peak force. Similar premature failure was observed when damage was calculated using Eqs. (11) and (12), in which damage rapidly accumulates from the early stages of loading. This damage accumulation in the ST specimen can be seen in Fig. 6c, in which contour plots of the compressive and tensile damage output variables DAMAGEC and DAMAGET, respectively, are shown for displacements D=0.18 mm and D=0.26 mm. It is noted that no contour plots are presented for the simulation using Eq. (13) at a displacement D=0.26 mm due to the exhibited premature failure at a much lower displacement. In contrast, when Eq. (11) is used, or no damage is taken into account, the displacement at which maximum load occurs is overpredicted compared to the experimental value due to the minor damage accumulation (Fig. 6c). When Eq. (14) is used to calculate d_c, the predicted strain at peak load is in accordance with the experimental observation. Based on these results, Eq. (14) was selected in this work to obtain the $d_c - \tilde{\varepsilon}_c^{in}$ curves for the CDP material model for the FE simulations of the different graphite grades. The values of n used in Eq. (14) for the IG-110, NBG-18 and PCEA graphite grades were 4.2, 3.5 and 4.0, while the values of ε_{cf} were 0.018, 0.012 and 0.017, respectively.

3.2. Optimisation process

Using the CDP material model to successfully predict nuclear-grade graphite's behaviour under compression and tension, i.e., matching the experimentally observed material response, requires finding an optimal set of the material model parameters. While several of these parameters described in Section 3.1 can be found through the experimental tests described in Section 2.2 (UC and ST tests) or in the literature, the dilation angle ψ is unknown for the studied graphite grades. Although a trial-and-error approach could be used to find an optimum value of ψ, i.e., manually trying different values of ψ until a satisfactory match between the predictions and measurements is achieved, this approach would be very time-consuming. It would also require previous experience or knowledge of reasonable values for the model parameter, which is not always available. Even in the best-case scenario, this approach may not find the optimal solution, which in most cases can only be obtained by finding the global minimum of the error function in an optimisation process.

For the multi-objective optimisation process in this work, the full-factorial design technique in the design of experiments (DOE) component of the optimisation software Isight 2024 [114] was used to find the optimum parameter ψ. The full-factorial design technique evaluates all combinations of all factors at all levels [114]. This optimisation process was chosen instead of using a genetic algorithm, for instance, considering that the parameter search space was finite (Table 3). For the

optimisation process in the Isight software, the Abaqus FE simulations (Section 3.1.1) were coupled with the optimisation component in an evaluation loop, automatically running through all the parameter values while evaluating their performance (fitness). This process performs fitness evaluation by comparing the predicted load-displacement curve with the experimentally measured average curve using objective functions. Here, two objective functions were employed, which are defined as:

$$\begin{cases} f_1 = \sum_{i=1}^{n} \left(P_{predicted} - P_{measured}\right)^2 \\ f_2 = \max\left\{\left|P_{predicted} - P_{measured}\right|\right\} \end{cases}, \quad (15)$$

where n is the number of points along the predicted and measured load-displacement curve, and P is either the predicted or measured load at a given point along the load-displacement curve. f_1 evaluates the sum of the squared difference (error magnitude) between all the points on the load-displacement curve. The second objective function, f_2, evaluates the maximum value of the absolute difference between the predicted and measured load.

In an ideal case, the same set of CDP's material model parameters should be able to describe the material's response under different loading conditions (UC and ST tests). However, for practical purposes, a set of parameters could also be found for a specific loading condition (compression loading, for instance) if a material or a structure is mainly subjected to a particular working load. To assess this difference, i.e., using a single set of parameters for both compression and tension loading or using two different sets of parameters, one for compression loading and one for tension loading, the optimisation process was performed in two different ways; that is, an optimisation of decoupled UC and ST models and an optimisation of coupled UC/ST models. For the decoupled optimisation, the optimisation was performed on the UC (Fig. 3a) and ST (Fig. 3b) models separately, using their corresponding average experimental load-displacement curve. This process leads to two different optimised ψ values, i.e., ψ_c for the UC loading condition (compression) and ψ_t for the ST loading condition (tension). For the optimisation of the coupled UC/ST models, the optimisation process was used to concurrently match the average experimental UC and ST load-displacement curves using a single value of ψ for both tested loading conditions, i.e., both UC and ST models were combined in a single FE model (Fig. 3c) and run simultaneously in the FE simulation. This process leads to an optimised ψ_{ct} for both UC and ST loading conditions. The optimisation processes were run using all the possible values of ψ shown in Table 3. For each optimisation process, i.e., decoupled UC model, decoupled ST model and coupled UC/ST models, the obtained optimal parameter ψ_c, ψ_t and ψ_{ct}, respectively, was selected as the best design point that resulted in the minimum sum of the objective functions [114]. The results of the optimisation processes are presented in Section 4.2.

4. Results and discussion

This section combines both the experimental and numerical results. The UC and ST experimental results are presented, including the force-displacement curves, obtained mechanical properties, and Weibull plots. DIC contours are presented to analyse the evolution of the strain fields during the ST test. The FE simulation results of the UC and ST tests using the CDP material model are also presented. The numerical results include presenting the numerical predictions using the different optimised values of ψ. Finally, this section presents a failure analysis based on experimental observations (failure modes) and numerical simulations showing the capability of the FE model with the CDP material model to predict the inelastic and fracture behaviour of nuclear graphite grades.

Table 3
Values of the dilation angle ψ for the optimisation process.

Parameter	Range	Increment	Number of possibilities
ψ	10.0–55.0 (°)	0.1	451

4.1. Mechanical testing

4.1.1. Mechanical properties

Fig. 7a–c present the recorded UC and ST experimental load-displacement curves for the IG-110, NBG-18 and PCEA graphite grades, respectively, while Table 4 summarises the material properties derived from the curves as mean ± standard deviation. The derived properties are the compressive yield strength σ_{cy}, the ultimate compressive strength σ_{cu}, the compressive strain-to-failure ε_{cu} taken as the strain at which the compressive strength is reached, and the splitting tensile strength σ_{tu}, which was calculated using Eq. (1). Note that σ_{cy} is determined as the stress at which the recorded load-displacement curves first visibly deviate from the linear elastic behaviour. As such, the determined compressive yield strength corresponds to the onset of micro-cracking, leading to inelastic strain. It can be seen from the results in Table 4 that the strength of the graphite grades is considerably greater in compression than in tension due to the significant tension-compression asymmetry of mechanical properties in graphite [130]. This difference in mechanical behaviour is explained as follows: during the ST test, the tensile stress field formed in the disc specimen due to the diametral compression loading provides a driving force for the growth (opening) of the pre-existing micro-cracks [42], which coalesce leading to macroscopic cracking, and ultimately fracture of the specimen. In contrast, the situation is different under compression, where the applied compressive load generates a significant compressive stress field across the cylindrical test specimen; these compressive stresses hinder the growth of micro-cracks, leading to significantly higher strength in compression for all graphite grades (Fig. 7a–c). The high compressive stresses can lead to the crushing of the material, which also contributes to the inelastic deformation and can be considered a deformation mechanism; however, only a limited amount of crushing was observed during UC tests of the graphite grades. While no crushing was observed during ST tests, it is possible that some crushing occurred in the form of compressive damage based on the numerical results, as discussed in Section 4.3.2.

The load-displacement responses of the tested graphite grades in Fig. 7a–c and the derived material properties summarized in Table 4 show that, on average, the fine-grained IG-110 and course-grained NBG-18 grades have a similar ultimate strength under both compressive and splitting tensile loading conditions. However, the IG-110 graphite curve (Fig. 7a–c) deviates from the linear elastic behaviour at a lower applied load during ST tests, which suggests an earlier onset of micro-cracking, pointing to the lower stability of the pre-existing micro-cracks. The medium-grained PCEA grade exhibits the lowest compressive yield strength and ultimate strength in both tension and compression loading conditions, thus suggesting the lowest stability of the pre-existing micro-cracks for this grade. On the other hand, the PCEA grade has an apparent higher ductility in compression compared to the NBG-18 grade, as indicated by ε_{cu} in Table 4, which could suggest a higher amount of crushing. Interestingly, the NBG-18 grade is noticeably more brittle than the other graphite grades as it fails at the lowest ε_{cu} in compression (Table 4) and also at the lowest displacement in tension (Fig. 7a–c).

As mentioned before, the IG-110 splitting tensile strength value obtained experimentally in this work (σ_{tu}=22.4 MPa, see Table 4) was much lower than most values of the IG-110 tensile strength found in the literature (25–30 MPa) [49,97,102]. A similar low value of σ_{tu}=21.8 MPa was obtained by Lin and Gallego [102] for the splitting tensile strength of the IG-110 grade. They attributed their results to the higher porosity and larger pores observed in the microstructure of the IG-110 grade compared to the other tested graphite in their work (Mersen 2114 grade) and the possible sample size effect. It is also possible that compressive damage occurred in the disc specimens during the ST tests

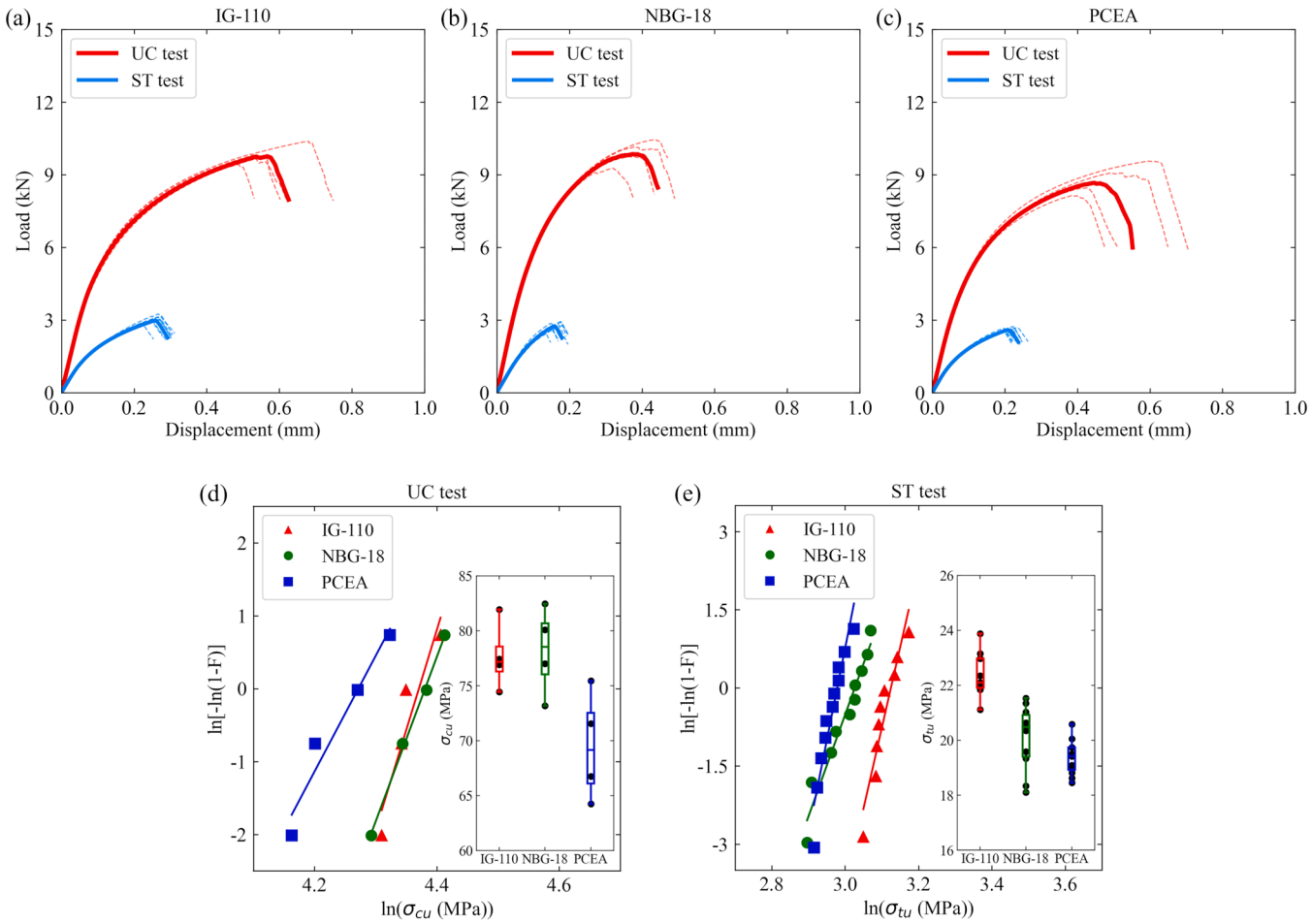

Fig. 7. Measured experimental load-displacement curves from the UC tests (red dashed lines) and the ST tests (blue dashed lines) for the (a) IG-110, (b) NBG-18, and (c) PCEA graphite grades; the average representative load-displacement curves are shown as solid lines. Weibull plots showing the rate of failure on the vertical axis and the selected failure criterion on the horizontal axis: (d) σ_{cu} for the UC test and (e) σ_{tu} for the ST test. The insets show a boxplot of the datasets.

Table 4
Material properties of the different graphite grades derived from the recorded experimental load-displacement curves shown in Fig. 7a–c, where σ_{cy} is the compressive yield strength, σ_{cu} is compressive ultimate strength, ε_{cu} is the compressive strain-to-failure, and σ_{tu} is the splitting tensile strength calculated using Eq. (1).

Graphite grade	σ_{cy} (MPa)	σ_{cu} (MPa)	ε_{cu} (-)	σ_{tu} (MPa)
IG-110	22.69 ± 1.97	77.67 ± 2.71	0.0309 ± 0.0040	22.37 ± 0.78
NBG-18	21.71 ± 3.95	78.18 ± 3.48	0.0203 ± 0.0030	20.80 ± 1.14
PCEA	14.99 ± 1.76	67.08 ± 6.17	0.0241 ± 0.0047	19.36 ± 0.61

[49], which is also suggested by the numerical results in this work (Section 4.3.2), producing a detrimental effect on the measured tensile strength. Notwithstanding these observations, the present results show that, on average, the fine-grained IG-110 grade exhibits a favourable combination of ultimate strength and ductility. It is noted that the coarse-grained NBG-18 grade performed similarly to the fine-grained IG-110 grade in terms of compressive and tensile strength; however, it showed noticeably reduced ductility in both compression and tension based on ε_{cu} (Table 4) and the displacement at peak load (Fig. 7a–c), respectively.

4.1.2. *Weibull analysis*

Fig. 7d–e show Weibull plots where the rate of failure is on the vertical axis, and the selected failure criterion, σ_{cu} for the UC test (Fig. 7d) and σ_{tu} for the ST test (Fig. 7e), is on the horizontal axis (see Table 4). The Weibull plots were obtained using the methodology described in Appendix A. Despite a limited number of experimental datasets, a good linear fit through the data is observed. In the analysis, the higher the Weibull modulus, the narrower the distribution of the selected failure criteria, which suggests lower measurement variability (Appendix A). For completeness, the datasets are also presented as boxplots (see insets in Fig. 7d–e). It can be seen in Fig. 7d–e that the medium-grained PCEA graphite consistently exhibited the lowest characteristic strength in both tension and compression. This graphite grade also exhibited the lowest Weibull modulus (large variability) in compression but showed the highest Weibull modulus (low variability) in tension. This observation suggests that the crack-initiating flaws in tension for the PCEA graphite were significant enough to result in a low characteristic strength but were also fairly consistent in size to give a high Weibull modulus. It can also be observed in Fig. 7d–e that the IG-110 and NGB-18 grades behave similarly in compression; however, the larger pores of the NGB-18 grade resulted in lower characteristic strength and Weibull modulus in tension; the large pores acted as crack initiation locations, and their variability in size (Fig. 1) led to a large scatter in the strength values. Overall, the fine-grained IG-110 graphite is the most predictable graphite grade as it has the highest Weibull module in compression and only a marginally worse Weibull modulus than the PCEA graphite in tension.

4.1.3. DIC measurements

Fig. 8 shows the DIC measurements recorded during the ST testing. Fig. 8a shows the evolution of the strain field in the X direction (perpendicular to the loading direction), while Fig. 8b shows the strain field in the Y direction (parallel to the loading direction). The DIC strain fields shown in Fig. 8 correspond to four distinctive locations along the force-displacement curve: **A** is the initial point, **B** is the mid-way displacement between **A** and **C, C** is the displacement at peak load, and **D** is a displacement after the peak load. The DIC contours reveal that the fine-grained IG-110 grade behaves like a single-phase homogeneous material exhibiting continuous and smooth strain fields. In contrast, the coarse-grained NBG-18 and the medium-grained PCEA grades are affected by the large pre-existing pores showing discontinuous strain fields. The effect of the pre-existing large pores is most apparent in the case of the NBG-18 grade, where these large pores act as strain concentrators, affecting the overall crack propagation. The discontinuous strain field is more pronounced for the NBG-18 grade, where the locations of high tensile strain concentration (red-coloured regions in Fig. 8a) are associated with the large pores.

The higher ductility of the IG-110 based on ε_{cu} (Table 4) and the displacement at peak load in the ST test (Fig. 7a–c), when compared to the NBG-18 and PCEA grades, can be explained in terms of its microstructure. The finer grain size of the IG-110 (Fig. 1a) allows this graphite grade to deform as a homogeneous material, as shown by the DIC continuous strain fields (Fig. 8). For instance, it can be seen in Fig. 8b that although the highest compressive strains are observed in the central region for all the graphite grades (indicated by the darkest blue-coloured area), it is clear that for the IG-110 graphite grade, the compressive strain is more globally distributed, reducing localised regions with high strain levels. This reduction in localised deformation due to its relatively homogenous microstructure, in turn, allows the IG-110 graphite to maintain its integrity through a higher level of deformation [82]. In addition, due to its lower Young's modulus, the IG-110 graphite grade requires the lowest level of applied stress for a given amount of elastic or inelastic deformation [99], contributing to its higher ductility.

On the contrary, the large pores observed in both NBG-18 and PCEA graphite grades (Fig. 1b and c) explain their lower ductility under both loading conditions compared to the IG-110 graphite grade. The pre-existing large pores acting as strain concentrators (Fig. 8) affect the overall crack propagation in these two graphite grades [38]. Moreover, the variability of the largest pore sizes found in the high-tension region for the NBG-18 grade (Fig. 8a) is expected to produce a large scatter in the tensile peak strength (Fig. 7e). Similar behaviour has been observed previously in the Gilsocarbon graphite [131]. In terms of compressive strength, while the IG-110 and NBG-18 have similar behaviour, the compressive strength of the PCEA grade is lower, notwithstanding the maximum grain size for the PCEA is smaller than that of the NBG-18 (Fig. 1 and Table 1). This lower compressive strength can be attributed to the less homogenous microstructure of the extruded PCEA graphite with a widespread distribution of flaws [99]. While the grain size and manufacturing process partly determine the strength, other factors related to the microstructure could be influencing the lower strength of the PCEA graphite grade [82]; however, a detailed study to address the structure-property relationships of the studied graphite grades is beyond the scope of this work.

4.2. FE simulations and optimisation results

Fig. 9a–f show the average experimental load-displacement curves from the UC test (red solid lines) and the ST test (blue solid lines), both labelled as Exp, along with the predicted load-displacement curves (labelled as Sim and shown as dashed or dotted lines) using different values of the parameter ψ, which was optimised by evaluating ψ values in the range of 10.0° to 55.0° (Table 3), as described in Section 3.2. As aforementioned, ψ was optimised for the three different graphite grades using two different optimisation processes: First, an optimisation process was used for decoupled UC and ST models to obtain the optimised values ψ_c and ψ_t, respectively (Table 5). Second, a coupled UC/ST model was used to obtain the optimised value ψ_{ct} (Table 5). Then, the optimised values ψ_c, ψ_t and ψ_{ct} were used individually in the CDP model of both UC and ST simulations to assess their effectiveness in predicting both the compressive and tensile behaviour of the graphite grades.

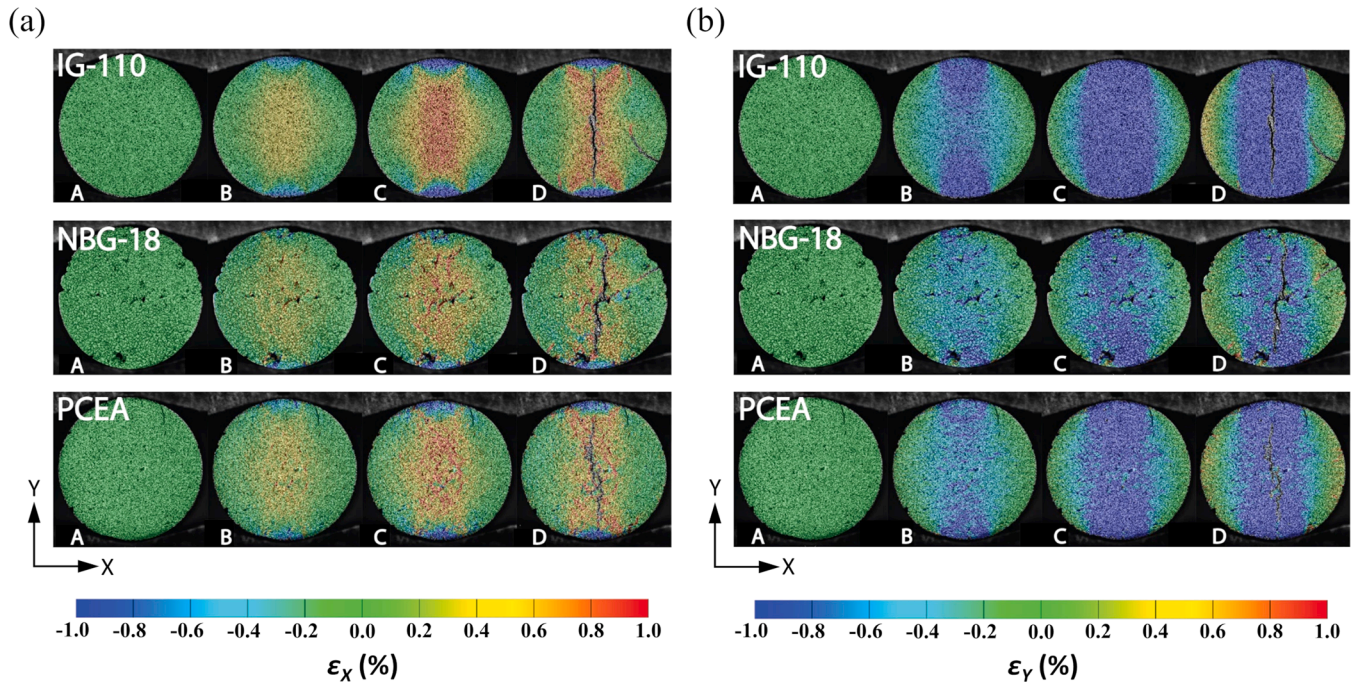

Fig. 8. DIC contours of (a) horizontal strain ε_X (normal to the applied load) and (b) vertical strain ε_Y (parallel to the applied load) of graphite grade disc specimens at different loading stages of the ST test. The **A, B, C** and **D** labels correspond to the following points along the ST force-displacement curves: **A** is the initial state, **B** is the mid-way displacement between **A** and **C, C** is the displacement at peak load, and **D** is a displacement after the peak load.

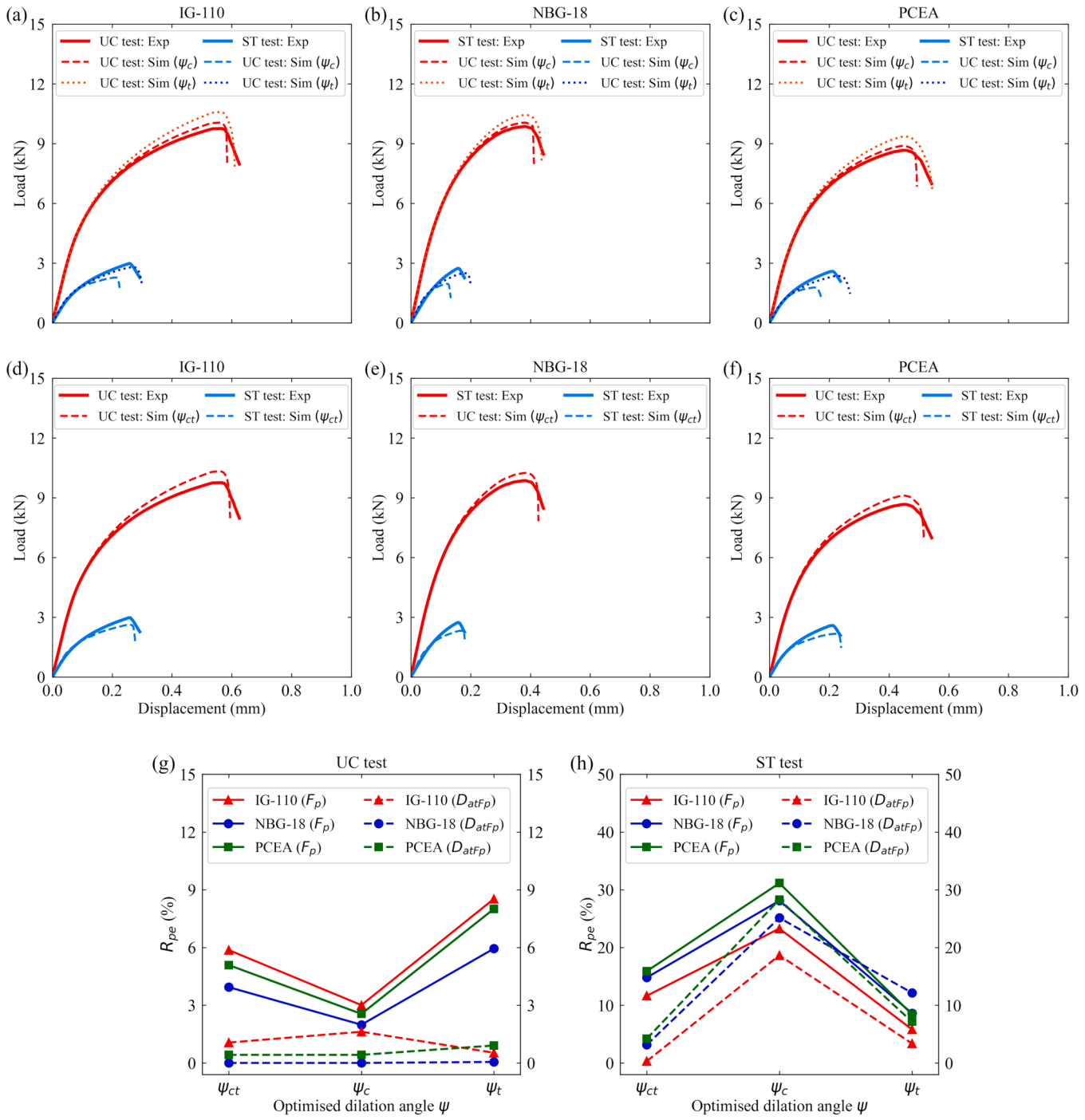

Fig. 9. Average experimental curves of UC and ST tests (solid lines) and predicted load-displacement curves from the FE simulations using different optimised ψ (dashed or dotted lines). Simulations using the values of either ψ_c or ψ_t in the UC and ST test models of the graphite grades (a) IG110, (b) NBG-18, and (c) PCEA. Simulations using the value of ψ_{ct} in UC and ST test models of the graphite grades (d) IG110, (e) NBG-18, and (f) PCEA. Relative percentage error R_{pe} of the predicted peak force F_p and the predicted displacement at peak force D_{atFp} for all the studied graphite grades using various values of ψ (ψ_c, ψ_t or ψ_{ct}) in the simulations of the (g) UC test and (h) ST test.

It can be seen in Table 5 that the optimised value for ψ_c was the lowest (10.0°) in the evaluated range for all graphite grades. This result can be explained considering two facts: (i) ψ has a positive effect on the compressive response of the material, i.e., higher values of ψ will result in higher peak force and ductility [132,133]; (ii) in all UC test simulations for all graphite grades, the CDP model tended to slightly overestimate the peak force compared to the experimental peak force. Thus, a value of ψ_c=10.0° reduces the predicted peak force, producing a better prediction of the UC test response (Fig. 9a–c). On the contrary, the optimised value for ψ_t was the highest in the evaluated range (55.0°) for the NBG-18 and PCEA grades and close to the highest for the IG-110 grade (53.3°). This result is explained by the fact that in all ST test simulations for all graphite grades, the CDP model slightly underestimated the peak force compared to the experimental ST peak force. Thus, a high value of ψ_t produces a better prediction of the ST test curve (Fig. 9a–c) by increasing the compressive resistance of the material, considering that the disc is subjected to compression stresses due to the diametral compression in the ST test. However, using the optimised ψ_c

Table 5
Optimised values of dilation angle ψ parameter of the CDP material model used in the simulations of studied graphite grades IG-110, NBG-18 and PCEA. ψ_c and ψ_t were obtained using decoupled UC and ST models, respectively. ψ_{ct} was obtained using coupled UC/ST models.

Graphite grade	ψ_c (°)	ψ_t (°)	ψ_{ct} (°)
IG-110	10.0	53.3	43.2
NBG-18	10.0	55.0	44.6
PCEA	10.0	55.0	43.6

for the ST test simulation will largely underestimate both the peak force F_p and the displacement at peak force D_{atFp} for all graphite grades (Fig. 9a–c, see blue dashed lines). Conversely, when ψ_t is used to predict the UC test behaviour, the simulation overpredicts the F_p much more than the prediction when using ψ_c for the UC test simulation (Fig. 9a–c, see red dotted lines).

The aforementioned differences in the predicted values can be seen better in Fig. 9g and h, in which the relative percentage error R_{pe} of F_p and D_{atFp} was used to compare the numerical predictions of the UC and ST tests, respectively, using the different optimised values of ψ. R_{pe} was calculated as:

$$R_{pe} = \frac{|v_{\text{sim}} - v_{\text{exp}}|}{v_{\text{exp}}} \times 100\%, \tag{16}$$

where v_{sim} is the predicted value of either P_p or D_{atFp}, while v_{exp} is the experimental value. In the case of the IG-110 graphite grade, when ψ_c is used, the model predicts better the compressive F_p (R_{pe}=3 %) and D_{atFp} (R_{pe}=1.6 %) as mentioned before (Fig. 9g); however, it vastly underestimates the F_p and D_{atFp} for the ST test with R_{pe} of 23.3 % and 18.6 %, respectively (Fig. 9h). In contrast, when ψ_t is used, the R_{pe} of the predicted F_p is below 10 % for both UC (8.5 %) and ST (5.8 %) tests, while the R_{pe} of the predicted D_{atFp} is 0.5 % and 3.4 % for the UC and ST

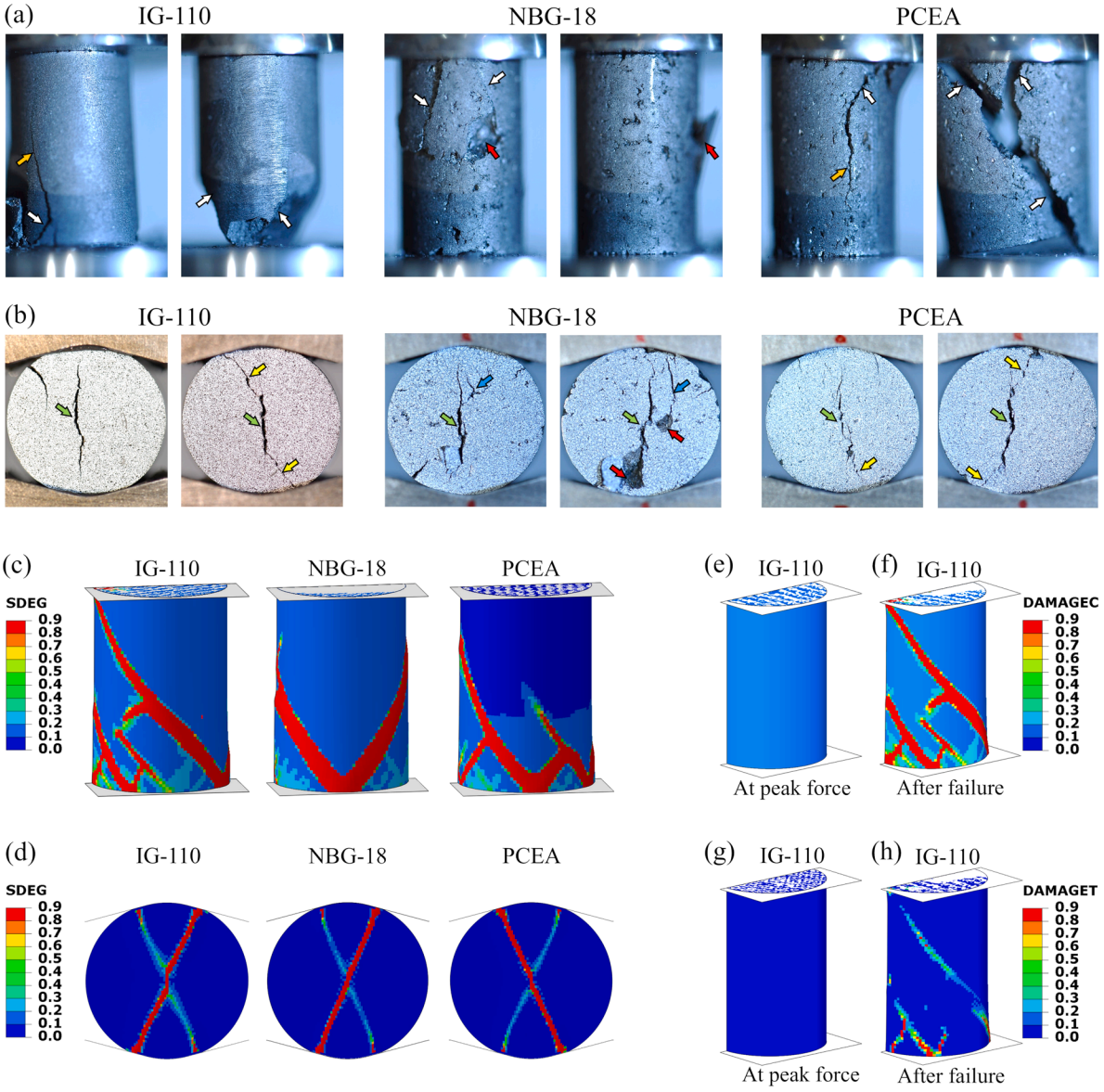

Fig. 10. Post-failure images of graphite specimens showing different failure modes: (a) for the UC test, the white arrows indicate shear cracks, the orange arrows show tension cracks, and the red arrows show spalling; (b) for the ST test, the green arrows show the primary tension crack, the yellow arrows show the primary crack growing towards the contact area of the specimen with the loading fixtures, the blue arrows show secondary cracks, and the red arrows show spalling. Contour plots of the damage variable SDEG after failure from the (c) UC and (d) ST test FE simulations of all the graphite grades. Contour plots of the compressive damage variable DAMAGEC from the UC test simulation of the IG-110 graphite grade: (e) at peak force and (f) after failure. Contour plots of the tension damage variable DAMAGET from the UC test simulation of the IG-110 graphite grade: (g) at peak force and (h) after failure.

tests, respectively. A similar trend was observed for the predicted values of F_p and D_{atFp} of the NBG-18 and PCEA graphite grades.

Regarding the results of the optimisation of the coupled UC/ST models, the optimised values of ψ_{ct} were in the range of 43.0° to 45.0° for all graphite grades (Table 5). These values produced the best prediction of the load-displacement curves for both the UC and ST test simulations (Fig. 9d–f). The results show that when ψ_{ct} is used to predict the mechanical behaviour of the IG-110 graphite grade, the CDP model predicts well the F_p for both UC (R_{pe}=5.8 %) and (R_{pe}=11.6 %) ST tests, while the R_{pe} of the predicted D_{atFp} is 1 % and 0.3 % for the UC and ST tests, respectively (Fig. 9g, h). Again, a similar trend was observed for the predicted values of F_p and D_{atFp} of the NBG-18 and PCEA grades when ψ_{ct} is used.

It is mentioned that using ψ_t also produces good predictions of F_p for both UC and ST tests with $R_{pe} < 10$ %; however, the better prediction of the F_p in the ST test when using ψ_t comes at the expense of larger R_{pe} of the D_{atFp}, that is, the predicted higher peak force in the ST test when using the larger value of ψ_t is the result of the specimen failing at a larger displacement due to the increased ductility of the material. Moreover, although a larger value of ψ can improve the prediction of the material's mechanical response [132], it may also adversely affect, due to the increased ductility, the post-failure response of the material, i.e., the failure modes and crack patterns [134]. Therefore, using ψ_{ct} for FE simulations of the graphite grades investigated here is recommended based on the results and discussion above.

4.3. Failure analysis

4.3.1. Experimental observations of failure modes

Fig. 10a and b show representative examples of graphite disc and cylindrical specimens after failure, showing the developed cracks and associated failure mechanisms. Two different specimens depicting the characteristic failure modes observed in the UC and ST tests are displayed in Fig. 10a and b, respectively, for each graphite grade. For the UC test (Fig. 10a), in all cases, the cracks initiated at one of the flat ends of the specimens (either the top or bottom flat end) due to high compressive stresses experienced in those regions. The developed macrocracks were mainly shear cracks, as expected in a uniaxial compression test of a cylindrical specimen, which has been previously observed in the compression testing of graphite [135] (indicated by the white arrows in Fig. 10a). Some of these macrocracks further propagated as tension cracks. i.e., they grew parallel to the loading direction (indicated by the orange arrows), which has also been previously observed in the uniaxial compression test of graphite [136]. Interestingly, spalling (small pieces of material detaching from the surface) was observed for the NBG-18 graphite grade (indicated by the red arrows in Fig. 10a), which is explained by the coalescence of cracks in compression [40] due to flaws or large pores in the NBG-18 grade compared to the other two graphite grades.

For the ST test (Fig. 10b), in all cases, the primary crack initiated at the centre of the specimen as expected due to the high tensile stresses in that region (Fig. 8a) and grew along the loading axis in the middle area of the specimen (indicated by the green arrows). It is noted that in some cases, the primary crack did not develop precisely at the centre line of the specimen, which is explained by the initial large imperfections (pre-existing voids) located in the middle region (but not along the centre-line) that may have acted as locations of stress concentration and thus locations of crack initiation and crack propagation. In some cases, after growing a certain length, the primary crack did not continue developing vertically along the loading direction; instead, the growing direction deviated towards the contact area of the specimen with the loading fixture (Fig. 10b), where high compressive stress developed (indicated by the yellow arrows); this secondary failure mode was observed in particular for the IG-110 and PCEA grades. Conversely, secondary cracks were observed for the NBG-18 (indicated by the blue arrows in Fig. 10b) as a secondary failure mode, which could result from the large voids in this course-grained graphite grade acting as stress concentrators and, thus, crack initiation locations. In addition, spalling was observed for the NBG-18 grade (indicated by the red arrows in Fig. 10b), which was also observed in the UC test of this graphite grade (Fig. 10a).

The failure modes observed in both compression and tension loading of the studied nuclear graphite grades, which are inherently quasi-brittle, showed that pre-existing defects and microcracks would significantly affect their fracture behaviour. When the graphite specimens are subjected to loading, pre-existing defects will grow, causing damage accumulation. The enlarged defects and microcracks will start interacting and eventually coalesce, forming macroscopic cracks [41,42]. Pre-existing defects can range in size from nanometres to several millimetres; this heterogeneity of defects across multiple length scales can lead to stress concentration related to the graphite's fracture behaviour [38]. As previously mentioned, the DIC contours (Fig. 8) showed that large pre-existing defects in the coarse-grained NBG-18 and the medium-grained PCEA grades resulted in discontinuous strain fields and acted as strain concentrators, affecting the crack propagation and failure modes. The pre-existing defects, which were significantly larger in NBG-18 graphite, resulted in spalling in both UC and ST tests and the formation of secondary cracks in the ST tests, showing the impact of pre-existing defects in the fracture behaviour of graphite.

4.3.2. FE simulations of the graphite behaviour after failure

FE simulations were performed in Abaqus/Explicit [113] to investigate the capability of the CDP model to predict the failure modes and crack development experimentally observed on the studied graphite grades subjected to the UT and ST tests. This explicit solver was selected for these particular simulations due to the material nonlinearity caused by the extensive plastic deformation developed in the specimens after the peak force and, in particular, after the failure (rapid decrease in the loading resistance), which caused the simulations in Abaqus/Standard, an implicit solver, to stop prematurely after the cracks started to grow rapidly due to convergence problems. Semi-automatic mass scaling was applied to the whole model to reduce computational time; a target time increment of 10^{-6} s was used. In addition, a half model was used instead of a quarter model to visualise better the crack growth in the simulation of the disc specimen subjected to the ST test, in which, based on the experiments, cracks can propagate on both sides of the centreline of the disc specimen surface after failure (Fig. 10b). All the material properties were the same as those used in the simulations presented in Section 4.2; however, the values of the optimised ψ_{ct} (Table 5) were used for all graphite grades.

Fig. 10c and d show the contour of the damage variable SDEG after failure from the UC and ST test FE simulations, respectively. It is mentioned that the output damage variable SDEG indicates the stiffness degradation d caused by both the compressive and tensile damage [113]. The output variable d, calculated internally by the FE software, is a function of the stress state and the uniaxial damage variables d_c and d_t and is defined as $(1 - d) = (1 - s_t d_c)(1 - s_c d_t)$, where s_t and s_c are functions of the stress state that are introduced to model stiffness recovery effects associated with stress reversals under uniaxial cyclic loading [113]. For the UC test simulations (Fig. 10c), it can be seen that for all graphite grades, the cracks initiated at the bottom flat end of the specimens due to high compressive stresses experienced in those regions, similar to the experimental observation (Fig. 10a). The predicted cracks were only shear cracks. It can also be seen in Fig. 10c that the behaviour of the NBG-18 graphite grade is predicted to be more brittle than the other two graphite grades, as only two prominent shear cracks were observed in the simulation of the UC test. This behaviour is further observed in Fig. 10d, where the ST test simulation is shown. For the NBG-18 graphite grade, the crack initiates in the middle of the specimen as expected; however, instead of first propagating parallel to the loading direction, it propagates towards the regions in contact with the loading fixtures. In contrast, in the ST test simulation of the IG-110 and PCEA graphite grades (Fig. 10d), the crack first propagates parallel to the

loading direction before propagating towards the areas in contact with the loading fixtures, as observed experimentally (Fig. 10b). It is noted that no secondary cracks or spalling was predicted for the NBG-18 graphite grade, as observed experimentally. This result is explained by the fact that the post-failure macroscopic behaviour of the NBG-18 is, in part, dictated by the large pores of the microstructure, which is not accounted for in the continuum-based FE simulations presented here.

Now, focusing on the numerical results of the fine-grained IG-110 graphite grade, which has the most homogenous microstructure of the studied graphite grades (Figs. 1 and 8), and thus, showed the least effect of pre-existing defects on the macroscopic mechanical response, Fig. 10e–h show the contour plots of the compressive damage variable d_c (DAMAGEC) and the tensile damage variable d_t (DAMAGET) at peak force and after failure from the UC test simulations. It is mentioned that d_c corresponds to the damage of the $d_c - \tilde{\varepsilon}_c^{in}$ curve obtained from Eq. (14), while d_t corresponds to the damage of the $d_t - \tilde{u}_t^{ck}$ curve obtained using Eq. (8), as explained in Section 3.1.4. It can be seen in Fig. 10e that at peak force, although no macrocracks have developed yet, the entire specimen has uniform compressive damage (light blue colour). In contrast, no tensile damage is observed (Fig. 10g), which is expected since the specimen is subjected to uniaxial compression. After failure, that is, when a sudden drop in the loading response occurs, cracks develop fast (Fig. 10f). Some tensile damage is also observed once the cracks have developed (Fig. 10h); however, compression damage is dominant (Fig. 10f).

Regarding the ST test simulations of the IG-110 graphite grade, Fig. 11a and b show the contour plots of the compressive damage variable damage d_c (DAMAGEC) and the tensile damage variable d_t (DAMAGET), respectively, at peak force, after peak force and after failure of the ST test simulation from the IG-110 graphite grade. It is mentioned that the damage contours after the peak force correspond to the part of the loading curve where the load has started to decrease, that is, between peak force and failure; at failure, a rapid decrease in loading resistance and catastrophic crack propagation occur. In both Fig. 11a and b, the damage contours are shown on the specimen front face and the symmetry plane surface (internal surface positioned at a distance equivalent to a half thickness from the front face of a complete specimen). In addition, damage contours on the cross-section and front face surfaces are shown in Fig. 11c.

It can be seen in Fig. 11b that at peak force, tensile damage has accumulated mainly in the middle section of the front face of the specimen, as expected due to tensile stresses perpendicular to the loading direction; however, some tensile damage is observed in a narrow region between the centre of the specimen and the area in contact with the loading fixtures. In contrast, no tensile damage is observed in the symmetry plane surface. Moreover, it can be seen in Fig. 11a that at peak force, considerable compressive damage has occurred in the regions where the specimen is in contact with the loading fixtures, while only minor compressive damage is observed in the central area of the symmetry plane surface.

After the peak force, a tensile crack started to develop in the middle of the specimen on the front face surface, growing parallel to the loading direction (Fig. 11b) as observed experimentally (Fig. 10b). Finally, after failure, the tensile crack fully developed and grew towards the areas in contact with the loading fixtures (Fig. 11b) as a result of the initial compression damage observed in those areas (Fig. 11a). Compressive damage is also observed in the crack path (Fig. 11a). Fig. 11c shows the damage in the specimen's cross-section after the peak force and after failure. It can be seen in the cross-section that the tensile damage initiates at the external front face surface and then develops towards the internal central region of the specimen, which has been observed in the splitting tensile behaviour of concrete [137].

These numerical results demonstrate that the FE simulations qualitatively match the failure modes, crack initiation and crack propagation of the graphite grades observed experimentally. However, the simulations predicted a more brittle behaviour than the observed experimentally for the coarse-grained NBG-18 graphite grade containing large pores, which exhibited localised strain concentrations not accounted for in the continuum-based FE simulations developed here. Nevertheless, the current results show that the employed CDP model predicts well the inelastic behaviour and peak force of the UC and ST tests for the three studied graphite grades and can also be used to predict reasonably well the failure modes, crack initiation and crack propagation of the fine-grained IG-110 and medium-grained PCEA graphite grades. It is,

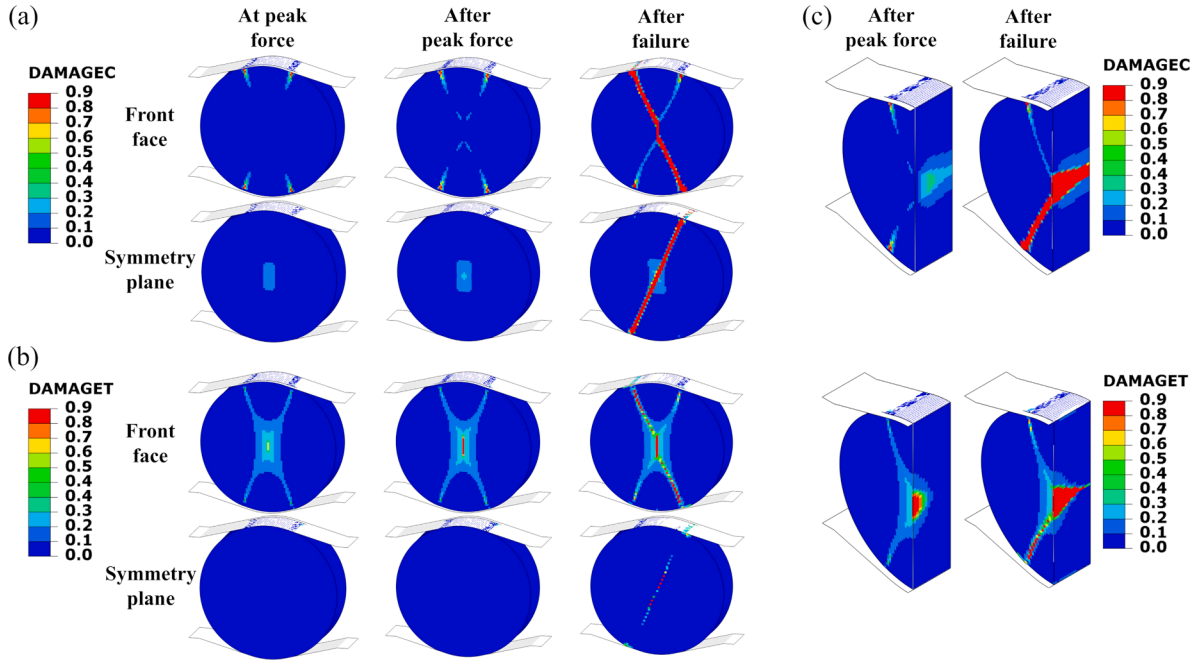

Fig. 11. Contour plots of the (a) compressive damage variable DAMAGEC and (b) tension damage variable DAMAGET from the ST test simulation of the IG-110 graphite grade at peak force, after peak force and after failure. (c) Contour plots of the damage variables DAMAGEC and DAMAGET after peak force and after failure on the cross-section surface.

however, acknowledged that further improvement to the model will need to be explored to account for the multi-scale nature of graphite containing various pre-existing defects and large pores, as these are known to affect the mechanical behaviour and fracture of nuclear-grade graphite.

5. Conclusions

This study has investigated the inelastic and fracture behaviour of three different nuclear graphite grades, fine-grained IG-110, coarse-grained NBG-18, and medium-grained PCEA, experimentally and numerically. The graphite grades were subjected to uniaxial compression (UC) and splitting tensile (ST) tests to experimentally compare their mechanical properties and failure mechanisms. In addition, the inelastic and fracture response was modelled using finite element (FE) simulations employing the concrete damaged plasticity (CDP) material model with an optimised dilation angle parameter. The main conclusions that can be drawn from this investigation are as follows:

The fine-grained IG-110 grade exhibited the most favourable combination of ultimate strength and ductility for both loading conditions, attributed to its relatively homogenous microstructure. In contrast, large pores in the coarse-grained NBG-18 and medium-grained PCEA grades acted as strain concentrators, affecting the overall macroscopic crack propagation, particularly for the NBG-18 grade.

The primary failure mode in compression was the development of several shear cracks; however, some tensile cracking was also observed. For the ST tests, specimens failed initially by a primary tensile crack initiated at the centre of the specimen propagating parallel to the applied load; however, in many instances, the crack further propagated towards the contact area of the specimen with the loading fixtures, where high compressive stress developed.

For the FE simulations employing the CDP material model, two different optimisation processes were used to select the CDP model's dilation angle parameter value, i.e., a decoupled optimisation performed on the UC and ST models separately and a coupled optimisation performed on the UC and ST models running simultaneously. The best predictions were obtained when the value from the coupled optimisation was used.

The numerical results showed that the CDP model can accurately capture the inelastic behaviour and peak force of the studied graphite grades under both UC and ST loading conditions. The FE simulations could also reasonably capture the failure modes observed experimentally in both UC and ST tests. In particular, the ST test model could capture the crack initiation and propagation path observed experimentally for the IG-110 and PCEA graphite grades.

In conclusion, the CDP material model successfully predicted the inelastic and fracture behaviour of nuclear graphite grades subjected to compression and tension loadings.

CRediT authorship contribution statement

K. Irman: Writing – original draft, Visualization, Methodology, Investigation, Formal analysis. **E.A. Flores-Johnson:** Writing – original draft, Visualization, Validation, Methodology, Investigation, Formal analysis. **J.J. Kruzic:** Writing – original draft, Supervision, Resources, Methodology. **W.E. Windes:** Writing – review & editing, Resources, Methodology. **T.J. Marrow:** Writing – review & editing, Resources, Methodology. **O. Muránsky:** Writing – original draft, Visualization, Validation, Supervision, Methodology, Investigation, Conceptualization.

Declaration of competing interest

The authors declare that they have no known competing financial interests or personal relationships that could have appeared to influence the work reported in this paper.

Acknowledgments

The authors would like to acknowledge the help of Mr Tim Palmer with the sample preparation and Mr Bruce Hudson with the in-house development of the DIC technique. We would also like to acknowledge the assistance of Mr David Carr and Dr Kevin Thorogood with the mechanical testing. Furthermore, we would like to thank Dr Thorsten Becker from Stellenbosch University for his advice on the numerical simulations. Finally, the authors would like to thank the Australian Institute of Nuclear Science and Engineering (AINSE) for financially supporting K. Irman through the Honours Scholarship.

Appendix A. Weibull analysis

The variability of the mechanical properties of brittle and quasi-brittle materials such as graphite can also be analysed using the Weibull probability distribution, which uses two fitting parameters: the shape parameter, which is the Weibull modulus (m), and the scale parameter, which is the characteristic strength (η). These two parameters describe the distribution of any measured material failure criteria [138]. The Weibull analysis is usually employed to predict the likelihood of brittle material failure while assuming that the probability of failure depends on the distribution of the weak regions where a crack initiates. The Weibull probability distribution is defined as [138]:

$$F = 1 - e^{-\left(\frac{\sigma_{us}}{\eta}\right)^m}, \tag{A1}$$

where F is the failure rate or cumulative failure probability, and σ_{us} is the measured ultimate strength. The Weibull modulus m describes the width of the distribution (variability), i.e., the higher the Weibull modulus, the narrower the distribution of selected failure criteria, pointing to small variably and high repeatability of the measured fracture stress. To determine both Weibull parameters (m and η), Eq. (A1) can be linearised as follows:

$$\ln[-\ln(1-F)] = m\ln(\sigma_{us}) - m\ln(\eta), \tag{A2}$$

where F can be calculated as $F = (n - 0.5)/N$; n is the rank (order) of individual measurements and N is the number of available measurements. The Weibull analysis can then be employed to determine what stresses will cause arbitrary failure rates when subjected to a given stress condition. As for any statistical methodology, the confidence in performing a statistical analysis depends on the amount of available data. The Weibull analysis was applied to this study's UC and ST test datasets by taking the strength as the material failure criterion in both loading conditions.

Data availability

Data will be made available on request.

References

[1] Zhou XW, Tang YP, Lu ZM, Zhang J, Liu B. Nuclear graphite for high temperature gas-cooled reactors. New Carbon Mater 2017;32:193–204. https://doi.org/10.1016/S1872-5805(17)60116-1.

[2] Moon J, Gallego NC, Contescu CI, Keiser JR, Sulejmanovic D, Zhang Y, Stringfellow E. A neutron tomography study to visualize fluoride salt (FLiNaK) intrusion in nuclear-grade graphite. Carbon 2023;213:118258. https://doi.org/10.1016/j.carbon.2023.118258. N Y.

[3] Fütterer MA, Strydom G, Sato H, Li F, Abonneau E, Abram T, Davies MW, Kim M, Edwards L, Muransky O, Pouchon MA, Yetisir M. The high temperature gas-cooled reactor. In: Greenspan E, editor. Encyclopedia of nuclear energy. Oxford: Elsevier; 2021. p. 512–22. https://doi.org/10.1016/B978-0-12-409548-9.12205-5.

[4] Campbell AA, Snead MA, Katoh Y. Understanding the effect of specimen size on the properties of fine-grain isotropic nuclear graphite for irradiation studies: physical, electrical, thermal properties. J Nucl Mater 2023;576:154269. https://doi.org/10.1016/j.jnucmat.2023.154269.

[5] Wilczopolska M, Suchorab K, Gawęda M, Frelek-Kozak M, Ciepielewski P, Brykała M, Chmurzyński W, Jóźwik I. Evolution of radiation-induced damage in nuclear graphite – A comparative structural and microstructural study. Diamond Relat Mater 2024;146:111247. https://doi.org/10.1016/j.diamond.2024.111247.

[6] Smith RE, Kane JJ, Windes WE. Determining the acute oxidation behavior of several nuclear graphite grades. J Nucl Mater 2021;545:152648. https://doi.org/10.1016/j.jnucmat.2020.152648.

[7] Burchell TD, Snead LL. The effect of neutron irradiation damage on the properties of grade NBG-10 graphite. J Nucl Mater 2007;371:18–27. https://doi.org/10.1016/j.jnucmat.2007.05.021.

[8] Barzilov A, Stewart J. Modeling of irradiated dimensional change strain in MSR graphite moderator. Nucl Eng Des 2023;407:112277. https://doi.org/10.1016/j.nucengdes.2023.112277.

[9] Marsden BJ, Haverty M, Bodel W, Hall GN, Jones AN, Mummery PM, Treifi M. Dimensional change, irradiation creep and thermal/mechanical property changes in nuclear graphite. Int Mater Rev 2016;61:155–82. https://doi.org/10.1080/09506608.2015.1136460.

[10] Karthik C, Kane J, Butt DP, Windes WE, Ubic R. Neutron irradiation induced microstructural changes in NBG-18 and IG-110 nuclear graphites. Carbon 2015;86:124–31. https://doi.org/10.1016/j.carbon.2015.01.036. N Y.

[11] Windes WE, Burchell TD, Davenport M. The advanced reactor technologies (art) graphite R&D program. Nucl Eng Des 2020;362:110586. https://doi.org/10.1016/j.nucengdes.2020.110586.

[12] Freeman HM, Mironov BE, Windes W, Alnairi MM, Scott AJ, Westwood AVK, Brydson RMD. Micro to nanostructural observations in neutron irradiated nuclear graphites PCEA and PCIB. J Nucl Mater 2017;491:221–31. https://doi.org/10.1016/j.jnucmat.2017.05.011.

[13] Yoon JH, Byun TS, Strizak JP, Snead LL. Characterization of tensile strength and fracture toughness of nuclear graphite NBG-18 using subsize specimens. J Nucl Mater 2011;412:315–20. https://doi.org/10.1016/j.jnucmat.2011.03.019.

[14] Liu D, Heard P, Nakhodchi S, Flewitt P. Small-scale approaches to evaluate the mechanical properties of quasi-brittle reactor core graphite. In: Tzelepi N, Carroll M, editors. Graphite testing for nuclear applications: the significance of test specimen volume and geometry and the statistical significance of test specimen population. West Conshohocken: ASTM International; 2014. p. 1–21. https://doi.org/10.1520/STP157820130127.

[15] Heard P, Wootton M, Moskovic R, Flewitt P. Crack initiation and propagation in pile grade A (PGA) reactor core graphite under a range of loading conditions. J Nucl Mater 2010;401:71–7. https://doi.org/10.1016/j.jnucmat.2010.03.023.

[16] Marrow T, Liu D, Barhli S, Mora LS, Vertyagina Y, Collins D, Reinhard C, Kabra S, Flewitt P, Smith D. *In situ* measurement of the strains within a mechanically loaded polygranular graphite. Carbon 2016;96:285–302. https://doi.org/10.1016/j.carbon.2015.09.058. N Y.

[17] Mostafavi M, Baimpas N, Tarleton E, Atwood R, McDonald S, Korsunsky A, Marrow T. Three-dimensional crack observation, quantification and simulation in a quasi-brittle material. Acta Mater 2013;61:6276–89. https://doi.org/10.1016/j.actamat.2013.07.011.

[18] Yu Z, Su RKL, Chen H, Shen J, Tsang DKL. Evaluations of J-integral of nuclear graphite combining experimental and numerical methods. Theor Appl Fract Mech 2023;128:104142. https://doi.org/10.1016/j.tafmec.2023.104142.

[19] Johns S, Windes WE, Rohrbaugh DT, Cottle DL. High temperature annealing of irradiated nuclear grade graphite. J Nucl Mater 2023;579:154377. https://doi.org/10.1016/j.jnucmat.2023.154377.

[20] Liu D, Gludovatz B, Barnard HS, Kuball M, Ritchie RO. Damage tolerance of nuclear graphite at elevated temperatures. Nat Commun 2017;8:15942. https://doi.org/10.1038/ncomms15942.

[21] Chi SH. Effects of specimen size on the flexural strength and weibull modulus of nuclear graphite IG-110, NBG-18, and PCEA. J Nucl Mater 2015;464:365–70. https://doi.org/10.1016/j.jnucmat.2015.04.053.

[22] Jiang M, Ell J, Barnard H, Wu H, Kuball M, Ritchie RO, Liu D. On the reduced damage tolerance of fine-grained nuclear graphite at elevated temperatures using *in situ* 4D tomographic imaging. Carbon 2024;222:118924. https://doi.org/10.1016/j.carbon.2024.118924. N Y.

[23] Liu D, Flewitt PE. Deformation and fracture of carbonaceous materials using *in situ* micro-mechanical testing. Carbon 2017;114:261–74. https://doi.org/10.1016/j.carbon.2016.11.084. N Y.

[24] Pagnoncelli AP, Paolino DS, Peroni L, Tridello A. Innovative tensile test for brittle materials: validation on graphite R4550. Int J Mech Sci 2024;261:108679. https://doi.org/10.1016/j.ijmecsci.2023.108679.

[25] Paraskevoulakos C, Roebuck B, Hallam KR, Flewitt PEJ. Temperature dependence of electrical resistivity, deformation, and fracture of polygranular graphite with different amounts of porosity. SN Appl Sci 2022;5:28. https://doi.org/10.1007/s42452-022-05243-1.

[26] Kane J, Karthik C, Butt DP, Windes WE, Ubic R. Microstructural characterization and pore structure analysis of nuclear graphite. J Nucl Mater 2011;415:189–97. https://doi.org/10.1016/j.jnucmat.2011.05.053.

[27] Snead LL, Contescu CI, Byun TS, Porter W. Thermophysical property and pore structure evolution in stressed and non-stressed neutron irradiated IG-110 nuclear graphite. J Nucl Mater 2016;476:102–9. https://doi.org/10.1016/j.jnucmat.2016.04.042.

[28] Arregui-Mena JD, Worth RN, Bodel W, März B, Li W, Campbell AA, Cakmak E, Gallego N, Contescu C, Edmondson PD. Multiscale characterization and comparison of historical and modern nuclear graphite grades. Mater Charact 2022;190:112047. https://doi.org/10.1016/j.matchar.2022.112047.

[29] Morrison CN, Zhang M, Jivkov AP, Yates JR. Discrete lattice model of quasi-brittle fracture in porous graphite. Mater Perform Charact 2014;3:414–28. https://doi.org/10.1520/MPC20130077.

[30] Freeman HM, Jones AN, Ward MB, Hage FS, Tzelepi N, Ramasse QM, Scott AJ, Brydson RMD. On the nature of cracks and voids in nuclear graphite. Carbon 2016;103:45–55. https://doi.org/10.1016/j.carbon.2016.03.011. N Y.

[31] Wen K, Marrow J, Marsden B. Microcracks in nuclear graphite and highly oriented pyrolytic graphite (HOPG). J Nucl Mater 2008;381:199–203. https://doi.org/10.1016/j.jnucmat.2008.07.012.

[32] Mrozowski S. Mechanical strength, thermal expansion and structure of cokes and carbons. In: Proceedings of the conferences on carbon; 1954. p. 31–45.

[33] Liu D, Mingard K, Lord OT, Flewitt P. On the damage and fracture of nuclear graphite at multiple length-scales. J Nucl Mater 2017;493:246–54. https://doi.org/10.1016/j.jnucmat.2017.06.021.

[34] Šavija B, Liu D, Smith G, Hallam KR, Schlangen E, Flewitt PE. Experimentally informed multi-scale modelling of mechanical properties of quasi-brittle nuclear graphite. Eng Fract Mech 2016;153:360–77. https://doi.org/10.1016/j.engfracmech.2015.10.043.

[35] Zhou Z, Bouwman WG, Schut H, Desert S, Jestin J, Hartmann S, Pappas C. From nanopores to macropores: fractal morphology of graphite. Carbon 2016;96:541–7. https://doi.org/10.1016/j.carbon.2015.09.069. N Y.

[36] Tang Y, Chen H. Characterization on crack propagation of nuclear graphite under three-point bending. Nucl Mater Energy 2019;20:100687. https://doi.org/10.1016/j.nme.2019.100687.

[37] Hodgkins A, Marrow T, Wootton M, Moskovic R, Flewitt P. Fracture behaviour of radiolytically oxidised reactor core graphites: a view. Mater Sci Technol 2010;26:899–907. https://doi.org/10.1179/026708309X12526555493477.

[38] Liu G, Tang Y, Hattar K, Wang Y, Windes W, Haque A, Du J. An investigation of fracture behaviors of NBG-18 nuclear graphite using *in situ* mechanical testing coupled with micro-CT. J Mater Res 2023;38:1984–93. https://doi.org/10.1557/s43578-023-00929-7.

[39] Shi L, Li H, Zou Z, Fok ASL, Marsden BJ, Hodgkins A, Mummery PM, Marrow J. Analysis of crack propagation in nuclear graphite using three-point bending of sandwiched specimens. J Nucl Mater 2008;372:141–51. https://doi.org/10.1016/j.jnucmat.2007.02.012.

[40] Xu J, Ma L, Xiao X, Wu D. Experimental study of the formation process and behaviors of spalling in rock materials. Eng Fail Anal 2023;143:106873. https://doi.org/10.1016/j.engfailanal.2022.106873.

[41] Yi Y, Xing T, Liu G, Sun L, Shi L, Ma S. Effects of tensile and compressive stresses on damage evolution law of nuclear graphite. J Nucl Mater 2023;583:154513. https://doi.org/10.1016/j.jnucmat.2023.154513.

[42] Becker TH, Marrow TJ, Tait RB. Damage, crack growth and fracture characteristics of nuclear grade graphite using the double torsion technique. J Nucl Mater 2011;414:32–43. https://doi.org/10.1016/j.jnucmat.2011.04.058.

[43] Lee JJ, Ghosh TK, Loyalka SK. Comparison of NBG-18, NBG-17, IG-110 and IG-11 oxidation kinetics in air. J Nucl Mater 2018;500:64–71. https://doi.org/10.1016/j.jnucmat.2017.11.053.

[44] Feng W, Qin M, Feng Y. Toward highly thermally conductive all-carbon composites: structure control. Carbon 2016;109:575–97. https://doi.org/10.1016/j.carbon.2016.08.059. N Y.

[45] Shi P, Chen Y, Wei Y, Feng J, Guo T, Tu Y, Sareh P. Deformation response of highly stretchable and ductile graphene kirigami under uniaxial and biaxial tension. Phys Rev B 2023;108:134105. https://doi.org/10.1103/PhysRevB.108.134105.

[46] Shi P, Chen Y, Feng J, Sareh P. Highly stretchable graphene kirigami with tunable mechanical properties. Phys Rev E 2024;109:035002. https://doi.org/10.1103/PhysRevE.109.035002.

[47] He R, Chen Y, Liang J, Sun Y, Feng J, Sareh P. Crystallographically programmed kirigami metamaterials. J Mech Phys Solids 2024;193:105903. https://doi.org/10.1016/j.jmps.2024.105903.

[48] Flores-Johnson EA, Townsend J, Wang Z, Reiner J, Kruzic JJ. Numerical simulations of the splitting tensile behaviour of needle-punched carbon/carbon

composites. J Compos Mater 2025. https://doi.org/10.1177/00219983251318603.
[49] Zhang X, Yi Y, Zhu H, Liu G, Sun L, Shi L, Jiang H, Ma S. Measurement of tensile strength of nuclear graphite based on ring compression test. J Nucl Mater 2018; 511:134–40. https://doi.org/10.1016/j.jnucmat.2018.09.010.
[50] Zhang C, Yuan Y, He Z, Tang H, Song J, Cai M, Tsang DKL, Zhou X. Determination of tensile strength by modified Brazilian disc method for nuclear graphite. Exp Tech 2020;44:475–84. https://doi.org/10.1007/s40799-020-00363-y.
[51] Ali M, Abbas S, de Azevedo ARG, Marvila MT, Khan MI, Rafiq W. Experimental and analytical investigation on the confinement behavior of low strength concrete under axial compression. Structures 2022;36:303–13. https://doi.org/10.1016/j.istruc.2021.12.038.
[52] Richard B, Ragueneau F, Cremona C, Adelaide L. Isotropic continuum damage mechanics for concrete under cyclic loading: stiffness recovery, inelastic strains and frictional sliding. Eng Fract Mech 2010;77:1203–23. https://doi.org/10.1016/j.engfracmech.2010.02.010.
[53] Chen X, Wu S, Zhou J. Influence of porosity on compressive and tensile strength of cement mortar. Constr Build Mater 2013;40:869–74. https://doi.org/10.1016/j.conbuildmat.2012.11.072.
[54] Xu L, Jiang L, Shen L, Gan L, Dong Y, Su C. Adaptive hierarchical multiscale modeling for concrete trans-scale damage evolution. Int J Mech Sci 2023;241: 107955. https://doi.org/10.1016/j.ijmecsci.2022.107955.
[55] Becker T, Marrow J. Modelling damage in nuclear graphite. In: Proceedings of the 13th international conference on fracture; 2013. June 16-21.
[56] Liu L, Li H, Zhang G, Fu S. Dynamic strength and full-field cracking behaviours of pre-cracked rocks under impact loads. Int J Mech Sci 2024;268:109049. https://doi.org/10.1016/j.ijmecsci.2024.109049.
[57] Yin X, Li Q, Wang Q, Chen B, Shu C, Xu S. Mesoscale numerical investigation of dynamic spalling fracture in toughness concrete. Int J Mech Sci 2024;264: 108826. https://doi.org/10.1016/j.ijmecsci.2023.108826.
[58] Cheng H, Paz CM, Pinheiro BC, Estefen SF. Experimentally based parameters applied to concrete damage plasticity model for strain hardening cementitious composite in sandwich pipes. Mater Struct 2020;53:78. https://doi.org/10.1617/s11527-020-01513-9.
[59] Neuberger YM, Andrade MV, de Sousa AMD, Bandieira M, da Silva Júnior EP, dos Santos HF, Catoia B, Bolandim EA, de Moura Aquino VB, Christoforo AL. de Araújo Ferreira M. Numerical analysis of reinforced concrete corbels using concrete damage plasticity: sensitivity to material parameters and comparison with analytical models. Buildings 2023;13:2781. https://doi.org/10.3390/buildings13112781.
[60] Sun S, Xu Q, Fan H, Xu Y, Wang X, Zhang Z. Damage characteristics and mechanical properties of CRTS III track structure in curved sections under longitudinal uneven subgrade settlement. Eng Fail Anal 2024;163:108607. https://doi.org/10.1016/j.engfailanal.2024.108607.
[61] Lubliner J, Oliver J, Oller S, Oñate E. A plastic-damage model for concrete. Int J Solids Struct 1989;25:299–326. https://doi.org/10.1016/0020-7683(89)90050-4.
[62] Lee J, Fenves GL. Plastic-damage model for cyclic loading of concrete structures. J Eng Mech 1998;124:892–900. https://doi.org/10.1061/(ASCE)0733-9399(1998)124:8(892).
[63] Hany NF, Hantouche EG, Harajli MH. Finite element modeling of FRP-confined concrete using modified concrete damaged plasticity. Eng Struct 2016;125:1–14. https://doi.org/10.1016/j.engstruct.2016.06.047.
[64] Yan JB, Zhang W. Numerical analysis on steel-concrete-steel sandwich plates by damage plasticity model: from materials to structures. Constr Build Mater 2017; 149:801–15. https://doi.org/10.1016/j.conbuildmat.2017.05.171.
[65] Qasem M, Hasan M, Muhamad R, Chin CL, Alanazi N. Generalised calibration and optimization of concrete damage plasticity model for finite element simulation of cracked reinforced concrete structures. Results Eng 2025;25:103905. https://doi.org/10.1016/j.rineng.2024.103905.
[66] Jin L, Zhang B, Chen F, Du X. CFRP-strengthened shear walls: combined effects of CFRP and reinforcement ratio. Int J Mech Sci 2024;282:109634. https://doi.org/10.1016/j.ijmecsci.2024.109634.
[67] Jin L, Zhang B, Chen F, Du X. Dynamic contribution of CFRP strips to CFRP-strengthened RC shear walls. Int J Mech Sci 2023;255:108479. https://doi.org/10.1016/j.ijmecsci.2023.108479.
[68] Zhang J, Li D, Huang B, Wang X, Jin L, Du X. Shear performance and size effect of CFRP strengthened RC beams. Int J Mech Sci 2024;267:109012. https://doi.org/10.1016/j.ijmecsci.2024.109012.
[69] Wang J, Jivkov AP, Li QM, Engelberg DL. Experimental and numerical investigation of mortar and ITZ parameters in meso-scale models of concrete. Theor Appl Fract Mech 2020;109:102722. https://doi.org/10.1016/j.tafmec.2020.102722.
[70] Albu-Jasim Q, Medina-Cetina Z, Muliana A. Calibration of a concrete damage plasticity model used to simulate the material components of unreinforced masonry reinforced concrete infill frames. Mater Struct 2022;55:36. https://doi.org/10.1617/s11527-021-01845-0.
[71] Scamardo M, Cattaneo S, Biolzi L, Vafa N. Parametric analyses of the response of masonry walls with reinforced plaster. Appl Sci 2022;12:5090. https://doi.org/10.3390/app12105090.
[72] Minghini F, Bertolesi E, Del Grosso A, Milani G, Tralli A. Modal pushover and response history analyses of a masonry chimney before and after shortening. Eng Struct 2016;110:307–24. https://doi.org/10.1016/j.engstruct.2015.11.016.
[73] Nastri E, Tenore M, Todisco P. Calibration of concrete damaged plasticity materials parameters for tuff masonry types of the Campania area. Eng Struct 2023;283:115927. https://doi.org/10.1016/j.engstruct.2023.115927.
[74] Wigger T, Lin B, Lupton C, Marrow J, Tong J. A 3D full-field study of cracks in a nuclear graphite under mode I and mode II cyclic dwell loading conditions. Fatigue Fract Eng Mater Struct 2020;43:1646–57. https://doi.org/10.1111/ffe.13183.
[75] Šavija B, Smith GE, Heard PJ, Sarakinou E, Darnbrough JE, Hallam KR, Schlangen E, Flewitt PEJ. Modelling deformation and fracture of gilsocarbon graphite subject to service environments. J Nucl Mater 2018;499:18–28. https://doi.org/10.1016/j.jnucmat.2017.10.076.
[76] Morrison CN, Jivkov AP, Vertyagina Y, Marrow TJ. Multi-scale modelling of nuclear graphite tensile strength using the site-bond lattice model. Carbon 2016; 100:273–82. https://doi.org/10.1016/j.carbon.2015.12.100. N Y.
[77] Xiong D, Tsang DKL. A multiscale modelling of polycrystalline nuclear graphite under effect of microcracks and incomplete-graphitized regions. J Mater Res 2023;38:675–85. https://doi.org/10.1557/s43578-022-00849-y.
[78] Liu G, Hattar K, Windes W, Haque A, Du J. Predicting and visualizing crack propagation in nuclear graphite. J Nucl Mater 2024;595:155056. https://doi.org/10.1016/j.jnucmat.2024.155056.
[79] Arregui-Mena JD, Griffiths DV, Worth RN, Torrence CE, Selby A, Contescu C, Gallego N, Edmondson PD, Mummery PM, Margetts L. Using porous random fields to predict the elastic modulus of unoxidized and oxidized superfine graphite. Mater Des 2022;220:110840. https://doi.org/10.1016/j.matdes.2022.110840.
[80] Zhang H, Huang YJ, Xu SL, Hu XJ, Zheng ZS. 3D cohesive fracture of heterogeneous CA-UHPC: a mesoscale investigation. Int J Mech Sci 2023;249: 108270. https://doi.org/10.1016/j.ijmecsci.2023.108270.
[81] Heijna MCR, de Groot S, Vreeling JA. Comparison of irradiation behaviour of HTR graphite grades. J Nucl Mater 2017;492:148–56. https://doi.org/10.1016/j.jnucmat.2017.05.012.
[82] Carroll MC, Windes WE, Rohrbaugh DT, Strizak JP, Burchell TD. Leveraging comprehensive baseline datasets to quantify property variability in nuclear-grade graphites. Nucl Eng Des 2016;307:77–85. https://doi.org/10.1016/j.nucengdes.2016.06.028.
[83] Locatelli G, Mancini M, Todeschini N. Generation IV nuclear reactors: current status and future prospects. Energy Policy 2013;61:1503–20. https://doi.org/10.1016/j.enpol.2013.06.101.
[84] Zhang X, Sun F, Xiong G, Xu W, Ding M. A review of research progress of graphite oxidation in high temperature gas-cooled reactors. Nucl Eng Des 2024;428: 113486. https://doi.org/10.1016/j.nucengdes.2024.113486.
[85] Sivan D, Meron E, Kinast S. Stability and bifurcation analysis of generation IV reactors via point reactor models with temperature reactivity feedback. Prog Nucl Energy 2023;160:104674. https://doi.org/10.1016/j.pnucene.2023.104674.
[86] Huang Q, Tang H. Porosity analysis of superfine-grain graphite IG-110 and ultrafine-grain graphite T220. Mater Sci Technol 2019;35:962–8. https://doi.org/10.1080/02670836.2019.1599557.
[87] Arai T, Sato S, Oku T, Schiffers H, Delle W. Assessment of heterogeneity and anisotropy of IG-110 graphite for nuclear components. J Nucl Sci Technol 1991; 28:713–20. https://doi.org/10.1080/18811248.1991.9731419.
[88] Cho KY, Kim KJ, Lim YS, Chung YJ, Chi SH. Specimen geometry effects on oxidation behavior of nuclear graphite. Carbon Sci 2006;7:196–200. https://www.dbpia.co.kr/journal/articleDetail?nodeId=NODE09612326.
[89] Arai T, Sato S, Oku T, Schiffers H, Delle W. Assessment of heterogeneity and anisotropy of IG-110 graphite for nuclear components. J Nucl Sci Technol 1991; 28:713–20. https://doi.org/10.1080/18811248.1991.9731419.
[90] Kane JJ, Matthews AC, Swank WD, Windes WE. Effects of air oxidation on the evolution of surface area within nuclear graphite and the contribution of macropores. Carbon 2020;166:291–306. https://doi.org/10.1016/j.carbon.2020.05.018. N Y.
[91] Huddleston BD, Mason TA, Gibson C, Angell C, Rasmussen N. Response of graphite to dynamic loading and hypervelocity jet impacts. New Orleans, Louisiana, USA: ASME 2023 International Mechanical Engineering Congress and Exposition; 2023. October 29-November 2.
[92] El-Genk MS, Tournier JMP. Comparison of oxidation model predictions with gasification data of IG-110, IG-430 and NBG-25 nuclear graphite. J Nucl Mater 2012;420:141–58. https://doi.org/10.1016/j.jnucmat.2011.09.027.
[93] Swank D, Lord J, Rohrbaugh D, Windes W. AGC-2 graphite preirradiation data package. Idaho Falls, ID, USA: Idaho National Laboratory; 2010. Technical Report INL/EXT-10-19588August.
[94] Burchell TD, Windes WE. USDOE ART graphite – selection and acquisition strategy. Oak Ridge, TN, USA: Oak Ridge National Laboratory; 2020. Technical Report ORNL/TM-2020/1591July.
[95] Olasov LR, Zeng FW, Spicer JB, Gallego NC, Contescu CI. Modeling the effects of oxidation-induced porosity on the elastic moduli of nuclear graphites. Carbon 2019;141:304–15. https://doi.org/10.1016/j.carbon.2018.09.051. N Y.
[96] Ishihara M, Sumita J, Shibata T, Iyoku T, Oku T. Principle design and data of graphite components. Nucl Eng Des 2004;233:251–60. https://doi.org/10.1016/j.nucengdes.2004.08.012.
[97] Jones KL, Laudone GM, Matthews GP. A multi-technique experimental and modelling study of the porous structure of IG-110 and IG-430 nuclear graphite. Carbon 2018;128:1–11. https://doi.org/10.1016/j.carbon.2017.11.076. N Y.
[98] Carroll MC, Rohrbaugh DT. Statistical comparison of the baseline mechanical properties of NBG-18 and PCEA graphite. Idaho Falls, ID, USA: Idaho National Laboratory; 2013. Technical Report INL/EXT-13-30011August.
[99] Carroll MC. Initial comparison of baseline physical and mechanical properties for the VHTR candidate graphite grades. Idaho Falls, ID, USA: Idaho National Laboratory; 2014. Technical Report INL/EXT-14-33120September.

[100] Chi SH. Specimen size effects on the compressive strength and weibull modulus of nuclear graphite of different coke particle size: IG-110 and NBG-18. J Nucl Mater 2013;436:185–90. https://doi.org/10.1016/j.jnucmat.2012.09.023.
[101] Carroll MC, Cottle DL, Rohrbaugh DT. Data report on the newest batch of PCEA graphite for the VHTR baseline graphite characterization program. Idaho Falls, ID, USA: Idaho National Laboratory; 2016. Technical Report INL/EXT-16-39604August.
[102] Lin L, Gallego NC. Effect of sample thickness on the tensile strength of small graphite discs. Oak Ridge, TN, USA: Oak Ridge National Laboratory; 2024. Technical Report ORNL/TM-2024/3403May.
[103] Albers TL. High-temperature properties of nuclear graphite. J Eng Gas Turbines Power 2009;131:064501. https://doi.org/10.1115/1.3093995.
[104] Su RKL, Chen HH, Fok SL, Li H, Singh G, Sun L, Shi L. Determination of the tension softening curve of nuclear graphites using the incremental displacement collocation method. Carbon 2013;57:65–78. https://doi.org/10.1016/j.carbon.2013.01.033. N Y.
[105] Chen HHN, Su RKL, Fok SL, Zhang HG. Fracture behavior of nuclear graphite under three-point bending tests. Eng Fract Mech 2017;186:143–57. https://doi.org/10.1016/j.engfracmech.2017.09.030.
[106] Burchell T, Erdmann IIID, Lowden RR, Hunter J, Hannel C. The fracture toughness of nuclear graphite grades. Oak Ridge, TN, USA: Oak Ridge National Laboratory; 2016. Technical Report ORNL/TM-2016/678November.
[107] ASTM D7012 - Standard Test Methods for Compressive Strength and Elastic Moduli of Intact Rock Core Specimens under Varying States of Stress and Temperatures. 2023. ASTM International. 10.1520/D7012-14E01.
[108] ASTM D8289 - Standard Test Method for Tensile Strength Estimate by Disc Compression of Manufactured Graphite. 2020. ASTM International. 10.1520/D8289-20.
[109] Li D, Wong LNY. The Brazilian disc test for rock mechanics applications: review and new insights. Rock Mech Rock Eng 2013;46:269–87. https://doi.org/10.1007/s00603-012-0257-7.
[110] Liu D, Zillhardt T, Earp P, Kabra S, Connolley T, Marrow T. *In situ* measurement of elastic and total strains during ambient and high temperature deformation of a polygranular graphite. Carbon 2020;163:308–23. https://doi.org/10.1016/j.carbon.2020.03.020. N Y.
[111] Wang Q, Jia X, Kou S, Zhang Z, Lindqvist PA. The flattened Brazilian disc specimen used for testing elastic modulus, tensile strength and fracture toughness of brittle rocks: analytical and numerical results. Int J Rock Mech Min Sci 2004;41:245–53. https://doi.org/10.1016/S1365-1609(03)00093-5.
[112] GOM Correlate 2021. Available online: https://www.gom.com/en/products/gom-suite (accessed on 28 June 2023).
[113] SIMULIA User Assistance. Abaqus 2024 documentation. Dassault Systèmes; 2024.
[114] SIMULIA User Assistance. Isight 2024 user's guide. Dassault Systèmes; 2024.
[115] ASTM D7219 - Standard Specification for Isotropic and Near-isotropic Nuclear Graphites. 2019. ASTM International. 10.1520/D7219-19.
[116] Hafezolghorani M, Hejazi F, Vaghei R, Jaafar MSB, Karimzade K. Simplified damage plasticity model for concrete. Struct Eng Int 2017;27:68–78. https://doi.org/10.2749/101686616X1081.
[117] Tao Z, Wang ZB, Yu Q. Finite element modelling of concrete-filled steel stub columns under axial compression. J Constr Steel Res 2013;89:121–31. https://doi.org/10.1016/j.jcsr.2013.07.001.
[118] Becker T. Understanding and modelling damage and fracture in nuclear grade graphite. Cape Town, South Africa: University of Cape Town; 2011. PhD thesis.
[119] Chira A, Puskás A, Bompa DV. Load-deformation response of long span prestressed concrete wide beams. J Build Eng 2023;65:105631. https://doi.org/10.1016/j.jobe.2022.105631.
[120] Al-Zuhairi AH, Al-Ahmed AH, Abdulhameed AA, Hanoon AN. Calibration of a new concrete damage plasticity theoretical model based on experimental parameters. Civ Eng J 2022;8:225–37. https://doi.org/10.28991/CEJ-2022-08-02-03.
[121] Vasudevamurthy G, Byun TS, Pappano P, Snead LL, Burchell TD. Effect of specimen size and grain orientation on the mechanical and physical properties of NBG-18 nuclear graphite. J Nucl Mater 2015;462:1–7. https://doi.org/10.1016/j.jnucmat.2015.02.012.
[122] Azadi Kakavand MR, Taciroglu E. An enhanced damage plasticity model for predicting the cyclic behavior of plain concrete under multiaxial loading conditions. Front Struct Civ Eng 2020;14:1531–44. https://doi.org/10.1007/s11709-020-0675-7.
[123] Anas SM, Alam M, Shariq M. Damage response of conventionally reinforced two-way spanning concrete slab under eccentric impacting drop weight loading. Def Technol 2023;19:12–34. https://doi.org/10.1016/j.dt.2022.04.011.
[124] Wahalathantri BL, Thambiratnam DP, Chan THT, Fawzia S. A material model for flexural crack simulation in reinforced concrete elements using ABAQUS. In: Proceedings of the first international postgraduate conference on engineering, designing and developing the built environment for sustainable Wellbeing (eddBE2011); 2011. 27-29 April.
[125] Zhou XQ, Kuznetsov VA, Hao H, Waschl J. Numerical prediction of concrete slab response to blast loading. Int J Impact Eng 2008;35:1186–200. https://doi.org/10.1016/j.ijimpeng.2008.01.004.
[126] Mazars J. A description of micro- and macroscale damage of concrete structures. Eng Fract Mech 1986;25:729–37. https://doi.org/10.1016/0013-7944(86)90036-6.
[127] Hu X, Guo W, Wang J, Yuan K. Damage growth-based constitutive model of satin weave composites under different temperatures and strain rates. J Appl Polym Sci 2019;136:47575. https://doi.org/10.1002/app.47575.
[128] Matzenmiller A, Lubliner J, Taylor RL. A constitutive model for anisotropic damage in fiber-composites. Mech Mater 1995;20:125–52. https://doi.org/10.1016/0167-6636(94)00053-0.
[129] Barhli SM, Saucedo-Mora L, Jordan MSL, Cinar AF, Reinhard C, Mostafavi M, Marrow TJ. Synchrotron X-ray characterization of crack strain fields in polygranular graphite. Carbon 2017;124:357–71. https://doi.org/10.1016/j.carbon.2017.08.075. N Y.
[130] Marsden BJ, Jones AN, Hall GN, Treifi M, Mummery PM. 14 - Graphite as a core material for generation IV nuclear reactors. In: Yvon P, editor. Structural materials for generation IV nuclear reactors. Woodhead Publishing; 2017. p. 495–532. https://doi.org/10.1016/B978-0-08-100906-2.00014-8.
[131] Mostafavi M, McDonald SA, Çetinel H, Mummery PM, Marrow TJ. Flexural strength and defect behaviour of polygranular graphite under different states of stress. Carbon 2013;59:325–36. https://doi.org/10.1016/j.carbon.2013.03.025. N Y.
[132] Mercan B, Schultz AE, Stolarski HK. Finite element modeling of prestressed concrete spandrel beams. Eng Struct 2010;32:2804–13. https://doi.org/10.1016/j.engstruct.2010.04.049.
[133] Rainone LS, Tateo V, Casolo S, Uva G. About the use of concrete damage plasticity for modeling masonry post-elastic behavior. Buildings 2023;13:1915. https://doi.org/10.3390/buildings13081915.
[134] Wosatko A, Winnicki A, Polak MA, Pamin J. Role of dilatancy angle in plasticity-based models of concrete. Arch Civ Mech Eng 2019;19:1268–83. https://doi.org/10.1016/j.acme.2019.07.003.
[135] Zhang C, He Z, Gao Y, Tang H, Qi W, Song J, Zhou X. The effect of molten FLiNaK salt infiltration on the strength of graphite. J Nucl Mater 2018;512:37–45. https://doi.org/10.1016/j.jnucmat.2018.09.051.
[136] Yi Y, Liu G, Xing T, Lin G, Sun L, Shi L, Ma S. Investigating the effects of confining pressure on graphite material failure modes and strength criteria. Nucl Eng Technol 2020;52:1571–8. https://doi.org/10.1016/j.net.2019.12.005.
[137] Jin L, Yu W, Du X, Yang W. Mesoscopic numerical simulation of dynamic size effect on the splitting-tensile strength of concrete. Eng Fract Mech 2019;209:317–32. https://doi.org/10.1016/j.engfracmech.2019.01.035.
[138] Weibull W. A statistical distribution function of wide applicability. J Appl Mech 2021;18:293–7. https://doi.org/10.1115/1.4010337.